Bulletin of the Seismological Society of America

New insights into long-period (>1s) seismic amplification effects in deep sedimentary basins: A case of the Po Plain basin of northern Italy

--Manuscript Draft--

Manuscript Number:	BSSA-D-20-00315R3
Article Type:	Article
Section/Category:	Special Section - Advances in Site Response Estimation
Full Title:	New insights into long-period (>1s) seismic amplification effects in deep sedimentary basins: A case of the Po Plain basin of northern Italy
Corresponding Author:	Claudia Mascandola INGV Milano, ITALY
Corresponding Author's Institution:	INGV
Corresponding Author E-Mail:	claudia.mascandola@ingv.it
Order of Authors:	Claudia Mascandola
	Simone Barani
	Marco Massa
	Dario Albarello
Abstract:	This study aims at investigating and quantifying the influence of the shallower deposits (down to few hundreds of meters) of the Po Plain sedimentary basin (northern Italy) on the long-period component (i.e., 1s < T < 3s) of seismic ground motion, where amplification effects due to the soft sediments above seismic bedrock were observed. A new seismo-stratigraphic model of the shallow deposits of the entire basin is provided with an unprecedented detail, by taking advantage of geophysical data recently acquired. The seismo-stratigraphic model is used to simulate the ground motion amplification in the Po Plain, by means of extensive 1-D ground response analysis. Results are compared with seismic observations available at a number of sites equipped with borehole seismic stations, where earthquakes have been recorded both at the surface and at the seismic bedrock depth. In spite of the general agreement with observations as concerns the seismic resonance frequencies, our model may fail in capturing the amplitude of the actual seismic amplification of the basin in the long-period range. We observe that 3-D basin effects related to surface waves generated at the edge of the basin may play a significant role in those zones where seismic hazard is controlled by distant sources. In these cases, 1-D modelling leads to average underestimations of 30 %, up to a maximum of 60%. The amplification functions need to be corrected for a basin-effects correction term, which in this case is provided by the ground motion prediction equation of the study area. These results should be taken into account in future seismic microzonation studies in the Po Plain area, where the 1-D approach is commonly adopted in ground response analyses, and in site-specific seismic hazard assessments aimed at the design of structures that are sensitive to the long-period component of seismic ground motion.
Author Comments:	I have addressed the remaining comments, provided by the Editor Thomas Pratt, which are included in the decision letter.
Suggested Reviewers:	Marco Pilz marco.pilz@gfz-potsdam.de Expert in strong motion and seismic noise analyses, engineering seismology, and site effects
	Giovanna Laurenzano glaurenzano@inogs.it Expert in numerical modelling of seismic wave propagation and site response estimation.
	Floriana Pergalani

	floriana.pergalani@polimi.it Expert in site response analyses for complex geological and morphological conditions.
	Alessandro Pagliaroli alessandro.pagliaroli@igag.cnr.it Expert in site effects and ground response analysis.
	Massimo Compagnoni massimo.compagnoni@polimi.it Expert in microzonation studies and site-effects.
	Chiara Smerzini chiara.smerzini@polimi.it Expert in ground motion simulations for seismic risk assessment.
	Chris Cramer ccramer@memphis.edu Expert in Seismic Strong Motion and Site Effects; Probabilistic Seismic Hazard and Risk Analysis.
Opposed Reviewers:	
Response to Reviewers:	I have addressed the remaining comments, provided by the Editor Thomas Pratt, which are included in the decision letter.
Additional Information:	
Question	**Response**
Key Point #1: <i>Three key points will be printed at the front of your manuscript so readers can get a quick overview. Please provide three COMPLETE sentences addressing the following: 1) state the problem you are addressing in a FULL sentence; 2) state your main conclusion(s) in a FULL sentence; and 3) state the broader implications of your findings in a FULL sentence. Each point must be 110 characters or less (including spaces).	We address the characterization of long-period site effects in the Po Plain sedimentary basin.
Key Point #2:	1D ground response analyses may underestimate the actual site amplification by up to 60%.
Key Point #3:	The 1D amplification functions need to be corrected using a basin-effects term from ground motion models.

New insights into long-period (>1s) seismic amplification effects in deep sedimentary basins: A case of the Po Plain basin of northern Italy

[(1)] Mascandola C., [(2)] Barani S., [(1)] Massa M., [(3)] Albarello D.

[(1)] Istituto Nazionale di Geofisica e Vulcanologia – Sezione di Milano, via Alfonso Corti 12, 20133 Milano (Italy).

[(2)] Dipartimento di Scienze della Terra, dell'Ambiente e della Vita (DISTAV), Università degli Studi di Genova, Corso Europa 26, 16132 Genova (Italy).

[(3)] Dipartimento di Scienze Fisiche, della Terra e dell'Ambiente (DSFTA), Università degli Studi di Siena, Via Laterina 8, 53100 Siena (Italy).

Email of corresponding author: claudia.mascandola@ingv.it

Declaration of Competing Interests

The authors acknowledge there are no conflicts of interest recorded.

Abstract

This study aims at investigating and quantifying the influence of the shallower deposits (down to few hundreds of meters) of the Po Plain sedimentary basin (northern Italy) on the long-period component (i.e., 1s < T < 3s) of seismic ground motion, where amplification effects due to the soft sediments above seismic bedrock were observed.

A new seismo-stratigraphic model of the shallow deposits of the entire basin is provided with an unprecedented detail, by taking advantage of geophysical data recently acquired. The seismo-stratigraphic model is used to simulate the ground motion amplification in the Po Plain, by means of extensive 1-D ground response analysis. Results are compared with seismic observations available at a number of sites equipped with borehole seismic stations, where earthquakes have been recorded both at the surface and at the seismic bedrock depth. In spite of the general agreement with observations as concerns the seismic resonance frequencies, our model may fail in capturing the amplitude of the actual seismic amplification of the basin in the long-period range. We observe that 3-D basin effects related to surface waves generated at the edge of the basin may play a significant role in those zones where seismic hazard is controlled by distant sources. In these cases, 1-D modelling leads to average underestimations of 30 %, up to a maximum of 60%. The amplification functions need to be corrected for a basin-effects correction term, which in this case is provided by the ground motion prediction equation of the study area. The corrected amplification functions are in agreement with the empirical observations, overcoming the uneven distribution of the recording stations in strong-motion datasets.

These results should be taken into account in future seismic microzonation studies in the Po Plain area, where the 1-D approach is commonly adopted in ground response analyses, and in site-specific seismic hazard assessments aimed at the design of structures that are sensitive to the long-period component of seismic ground motion (e.g., long-span bridges and tall buildings).

Keywords: Po Plain, seismo-stratigraphic model, 1-D ground response analysis, long-period soil amplification

Introduction

The importance of long-period (> 1 s) component of seismic ground motion has been recognized worldwide during some strong earthquakes occurred in the past (e.g., 1985 Michoacan M_W 8.1 (Furumura et al., 1998); 1994 Northridge M_W 6.7 (Davis et al., 2000); 1999 Hector Mine M_W 7.1 (Grazier et al., 2002); 2002 Denali M_W 7.9 (Ratchkovski et al., 2003); 2003 Tokachi-oki Mw 8.0 (Miyazaki et al., 2004)). Significant damage to long-period structures at large hypocentral distances, as well as prolonged duration of seismic ground-motion, focused the attention of seismologists on soil amplification effects in deep sedimentary basins. The characteristics of long-period ground motion have gained growing interest also in the civil engineering community because of the increasing number of large structures, such as tall buildings, long-span bridges, large storage tanks and seismically isolated structures (Koketsu and Miyake, 2008). In these cases, long-period site response modelling is crucial for risk mitigation strategies, especially when several civil and strategic infrastructures (e.g., nuclear power plants, high-speed railway) are present.

Long-period ground motion amplification is a relevant issue in the Po Plain (northern Italy; Figure 1), which is one of the deepest and widest sedimentary basins worldwide, as it covers an area of about 50,000 km^2 and presents Plio-Quaternary sediments that can reach about 9 km thickness in the Apennine foredeep (e.g., Burrato et al., 2003; Toscani et al., 2009). In this area, long-period resonance phenomena have been well-documented by many studies (e.g., Priolo et al., 2012; Luzi et al., 2013; Milana et al., 2013; Martelli and Romani, 2013; Massa and Augliera, 2013; Paolucci et al., 2015a; Tarabusi and Caputo, 2017; Mascandola et al., 2017; Laureanzano et al., 2017). However, most of these studies focus on the epicentral area of the 2012 Emilia seismic sequence, where significant ground-motion amplification and increased duration were observed (e.g., Luzi et al., 2013). A recent study of Mascandola et al. (2019) mapped long-period resonance phenomena in the whole Po Plain, by means of extensive ambient-vibration measurements performed throughout the basin. Resonance effects ranging between 1-3 s are caused by a marked increase in the mechanical properties of the

Quaternary continental deposits, at the contact between soft and relatively stiff materials within the sedimentary sequence. This seismic impedance contrast identifies the seismic bedrock depth in the Po Plain area (Figure 1, Mascandola et al., 2019).

Since basin stratigraphy and buried morphology play a fundamental role on ground motion amplification, detailed knowledge of 3-D crustal structure is a key element in understanding seismic wave propagation processes. In this regard, several 3-D seismic velocity models were developed for the Po Plain in order to reproduce the observed ground motion and predict the effects of its complex geological structure. One of the first attempts was that of Vuan et al. (2011), who simulated the long-period ($T > 5$ s) surface waves generated in the basin by strong ($M_W > 6$) earthquakes. More recently, Molinari et al. (2015) set up a more complex 3-D model (known as MAMBo), suitable for seismic wave propagation at $T > 3$ s. Another model is the one developed by Paolucci et al. (2015b), in the epicentral area of the 2012 Emilia seismic sequence, to simulate the near-source strong motion associated with the M_W 5.8 20 May 2012 earthquake. In a nearby area, Klin et al. (2019) proposed a more detailed 3-D model (called ER3D) suitable for seismic wave propagation at $T > 0.5$ s. Besides the above-mentioned studies, it is worth mentioning the one developed within the framework of the European GeoMol Project (GeoMol Team, 2015). This is a 3-D model of the central plain that was defined with the aim of assessing the subsurface potentials (e.g., geothermal potential and storage potential for fluids) of the Alpine foreland basins. These models represent the reference for numerical simulations that can help to better understand and estimate the characteristics of long-period ground motion in the Po Plain. However, all these models lack a detailed characterization of the shallower geology (i.e., first hundreds of meters), where a fixed shear-wave velocity (*Vs*) value is set throughout the study area.

This work presents an attempt to account for heterogeneities in the *Vs* profile of these deposits, which are expected to play a major role on soil amplification at long and intermediate periods (e.g., Parolai, 2012; Barani et al., 2013). While Mascandola et al. (2019) defined the buried morphology of the

seismic bedrock for the entire Po Plain area (Figure 1), a large-scale shear-wave velocity model for the soft sediments above it is still missing. This work proposes a new seismo-stratigraphic model for the sedimentary cover down to the seismic bedrock depth (i.e., first hundreds of meters), by means of 3-D interpolation of several shear-wave velocity profiles obtained from microtremor array measurements and borehole tests. To this end, the extensive ambient-vibration dataset of Mascandola et al. (2019) is considered, along with additional ambient-vibration analyses provided by the Geological Survey of the Emilia-Romagna Authority (see Data and Resources). This yields a grid of 1-D soil models covering the entire Po Plain. Ground response is then evaluated through 1-D equivalent linear numerical analyses, considering the input motion selected by Mascandola et al. (2020). In that study, a clustering analysis of the regional seismic hazard is applied to define a set of target spectra then used as benchmark in the selection of the acceleration time histories (readers interested in the details of the selection procedure may refer to Mascandola et al. (2020); the selected time histories are provided therein). The consistency of 1-D numerical amplification functions is evaluated by comparison with seismic observations at a set of sites where earthquake recordings are available both at surface and at seismic bedrock level. Finally, the 1-D assumption is discussed by comparing the numerical (normalized) response spectra with ones at the ground surface, and comparing the amplification functions obtained in this study with those provided by region-specific ground motion prediction equation (Lanzano et al., 2016).

Seismo-stratigraphic model

With the aim of providing a shear-wave velocity model down to the seismic bedrock, all available shear-wave velocity (*Vs*) profiles from microtremor arrays and borehole tests (cross-hole and down-hole) in the study region are considered. 48 shear waves velocity(*Vs*) profiles are selected (Figure 1): 32 out of them are from the dataset considered in Mascandola et al. (2019) to model the seismic

bedrock morphology in the Po Plain, and 16 are additional *Vs* profiles provided by the Geological Survey of the Emilia-Romagna Authority (see Data and Resources). Specifically, 60% of the *Vs* profiles collected by Mascandola et al. (2019) derive from numerical inversion of ambient-vibration array data, which were acquired and processed within the framework of projects aimed at the geophysical characterization of some sites hosting the permanent seismic stations of the National Seismic Network (RSN, see Data and Resources) and Italian Accelerometric Network (RAN, see Data and Resources) (e.g., Bordoni et al., 2017). The remaining 40% of *Vs* profiles were provided by the Geological Survey of the Emilia-Romagna Authority (see Data and Resources). As with additional 16 *Vs* profiles included in this work, they were determined from pre-analyzed ambient-vibration array data acquired for seismic microzonation studies in the Emilia-Romagna region. The selected *Vs* profiles present an uneven distribution over the study area (Figure 1), with an inter-distance that ranges from 3 km in the central plain to 30 km toward West. Consequently, a different spatial resolution characterizes different areas of the model. However, the Po Plain sedimentary basin is relatively homogeneous as concerns the regional-scale sedimentation process, and lateral variations in the *Vs* profile are expected to be smooth (e.g., Regione Emilia-Romagna, ENI–AGIP, 1998; Regione Lombardia, Eni Divisione Agip, 2002; Muttoni et al., 2003; Scardia et al., 2012; Martelli et al., 2017).

A 3-D shear-wave velocity model down to the seismic bedrock depth is generated by interpolating the selected *Vs* profiles. To this end, each *Vs* profile is discretized in a set of points spaced by 1 m, each of which is defined by a depth value *z* (in m) and a value of *Vs* (in m/s). The interpolation is computed by means of an inverse distance weighting (IDW) algorithm, with a weighting exponent of 2 and a cutoff distance of 32 km (10% of diagonal extent of gridded area). The 3-D model is discretized in *voxels* with a vertical resolution of 5 m and a horizontal resolution of 524x524 m. Finally, a smoothing algorithm that consists in a voxel averaging within a smoothing window (2

voxels both in the horizontal and vertical directions), is applied. Figure 2a shows the seismo-stratigraphic model through N-S and E-W perpendicular sections.

Three layers have been identified based on the *Vs* thresholds defined in the current seismic codes (European Committee for Standardization, 2004; Ministero delle Infrastrutture e dei Trasporti, 2018) for soil classification. The shallower layer of the model, with thickness up to 20 m and values of *Vs* that are lower than 180 m/s, is located eastward (Figure 2b). The deeper layer, which presents V_S values between 180 and 360 m/s, reaches 25 m depth towards West and deepens down to 175 m eastward (Figure 2c). The deeper structure of the model presents higher velocities (in the range of 360-800 m/s), with the same eastward decreasing trend observed in the shallower sediments. The bottom of this deeper layer marks the bedrock depth (Figure 1), where V_S is set to 800 m/s.

In Figure 3, we compare the seismic velocity model developed here with those available for the Po Plain area (i.e., Molinari et al., 2015; Paolucci et al., 2015b; GeoMol Team, 2015; and Klin et al., 2019), both in terms of extension (Figure 3a) and in terms of *Vs* distribution (Figure 3b-e). Specifically, for the area of Mirandola, which is common to all these models, we provide N-S cross-sections (trace A-A' in Figure 3a) showing the lateral distribution of *Vs*. It is evident that, compared to the models mentioned above, which assign a uniform *Vs* value to the shallow deposits, the seismo-stratigraphic model proposed here allows an unprecedented detail in the distribution of *Vs*, taking advantage of recent site characterization and seismic microzonation studies in the Po Plain area.

Seismic Modelling of 1-D Site Response

Soil Modeling

The study area is discretized into a 0.1° x 0.1° grid. For each node, a discrete *Vs* profile is defined from the shear-wave velocity model in Figure 2. In this discretization, the thickness of each layer increases with depth according to a geometric progression, of the form of:

$$z_n = z_0 r^{n-1} \quad (2)$$

where z_n is the depth of the bottom of *n*-th layer with $n > 1$, $z_0 = 5$ m is the depth of the first layer, and $r = 2$. A value of V_S is then assigned to each layer. It corresponds to the average shear-wave velocity computed from the model in Figure 2, in the depth range of the layer for the relevant vertical profile. The shear wave velocity of the seismic bedrock is set to 800 m/s. Unit weight is assigned by using the empirical relation proposed by Mayne (2001), which is defined as a function of *Vs* and depth for all types of saturated geomaterials, ranging from clays to gravel to rocks:

$$\gamma = 8.32log(Vs) - 1.61log(z) \quad (3)$$

where γ is the saturated unit weight in kN/m^3, *Vs* is the shear-wave velocity in m/s, and *z* is the depth in meters. As regards modulus reduction and damping curves, the depth-dependent models proposed by EPRI (1993) are adopted for the soil deposits, whereas the curves of Schnabel (1973) are considered for the bedrock. Note that these latter were calibrated for *Vs* > 900 m/s, slightly above the threshold adopted in this study (i.e., 800 m/s). For the soil deposits, we adopt the degradation curves of EPRI (1993) mainly because of the scale of the study (regional scale) and unavailability of specific degradation curves, particularly for sediments at large depths. In order to examine the sensitivity of the results to such curves (i.e., soil nonlinear behavior), we compared the results obtained from equivalent-linear and fully linear analyses for a number of sites (not shown for the sake of brevity). The comparison reveals negligible differences (generally less than 10%, only for T < 0.05s), thus indicating that results are basically insensitive to the choice of the curves adopted. This is in agreement with the results of Kaklamanos et al. (2013; 2015) and Zalachoris and Rathje (2015) showing that, for the long-period range (> 1s), the difference between equivalent-linear and non-linear approaches is negligible. It is worth noting, however, that in the case of site-specific studies

aimed at the design of critical structures, for which long return periods (i.e., severe seismic loading) have to be considered over a wide range of periods, the use of nonlinear approaches is advisable.

The uncertainty in the soil properties is considered by applying the method described in Bazzurro and Cornell (2004) and Barani et al. (2013), which consists in randomly varying the values of the soil properties via Monte Carlo simulation. The uncertainty in modulus reduction and damping curves is modeled by varying the shear strain value ($\varepsilon_{64\%}$ at 64% of the shear modulus ratio (*G/Gmax*). This random variable (*RV)*, as well as shear-wave velocity *Vs* and layer depth *z*, is considered lognormally distributed with a given mean and standard deviation ($\sigma_{\ln RV}$). At each node, we assume $\sigma_{ln\varepsilon_{64\%}}$ = 0.35 (Bazzurro and Cornell, 2004), σ_{lnV_S} = 0.1 (which roughly corresponds to assuming a 10% variability on *Vs*), and σ_{lnz} = 0.13 according to the empirical regression model defined in Mascandola et al. (2019). The uncertainty in γ is not considered, as its influence on soil amplification was shown to be negligible (e.g., Barani et al., 2013). All distributions are truncated at ± $2\sigma_{\ln RV}$ to prevent unrealistic values. Finally, we assume that the bedrock velocity is not lower than 750 m/s, and that the shear-wave velocity of sedimentary deposits monotonically increases with depth (i.e., velocity inversions are not allowed). For each grid node, 100 soil profiles are generated via Monte Carlo simulation. As an example, Figure 4 shows the randomized models for a node of the study area. The variability of shear modulus reduction and damping curves is shown in Figure 5.

1-D Ground Response Analyses

The ground response analyses are performed by using Shake91 (Idriss and Sun, 1993), which implements an equivalent linear approach to model the nonlinear response of soils. The seismic excitation adopted in this study is that provided by Mascandola et al. (2020). Different sets of twenty natural accelerograms (relative to the two horizontal ground motion components of ten earthquakes), are considered for different zones of the Po Plain, each including nodes with similar seismic hazard

levels (see Mascandola et al. 2020 for further details). The accelerograms are selected at the reference soil conditions of $V_{S,30}$ > 750 m/s. We assume a negative tolerance of 50 m/s with respect to the standard definition (i.e., $V_{S,30}$ = 800 m/s) given in the European and Italian norms (European Committee for Standardization, 2004; Ministero delle Infrastrutture e dei Trasporti, 2018). This leads to 2000 numerical simulations (20 accelerograms x 100 soil model randomizations) for each node of the computation grid. Note that, for a given earthquake, the response spectra corresponding to the two horizontal components are combined by taking the envelope of the maximum accelerations (e.g., Barani et al., 2015). Thus, for each grid node, we get 10 response spectra at the outcropping bedrock and 1000 spectra at the soil surface. The features of each ground motion recording (e.g., *PGA*, *PGV*), along with those of the associated earthquakes (e.g., magnitude, source-to-site distance), are listed in Table S1 of the electronic supplement. Considering the values of the strain index I_γ (e.g., Idriss, 2011) associated with the selected input motions (Table S1), which are always less than 0.02%, and the results of Kim et al. (2016), soil non-linearity can be actually neglected (i.e., there is no need of using computer codes that fully account for soil nonlinearity, being the linear equivalent approach sufficient for our purposes).

The ground motion amplification due to the soft sediments above seismic bedrock is quantified here by the amplification function, *AF(f)*, defined as the ratio of the soil spectral acceleration to the bedrock spectral acceleration (corresponding to the rock-outcropping motion driven at the base of each model). Given the target of this study, we focus on the long-period component of ground motion at 1-3 s, within which amplification effects due to the soft sediments above seismic bedrock have been observed (Mascandola et al. 2019).

The results of the ground response analyses are shown in Figure 6 in terms of median *AF(f)* values, obtained by 1000 Monte Carlo realizations. Figure 6 shows that the median values of *AF(f)* vary between 1 and 3, with an eastward increase regardless of period. This is related to the eastward dipping of the seismic bedrock that induces amplifications down to a period of 3 s toward the Adriatic coast (Mascandola et al., 2019). Figure 6 also shows that the maximum amplification occurs in

241 different part of the basin depending on period. At 1 s, the maximum amplification concentrates
242 northeast of Casaglia, with values up to 2.5-3.0 (Figure 6a). At longer periods (1.25-1.67 s), the
243 maximum amplification concentrates in a small area near Casaglia and in a slightly wider area to the
244 southeast (Figure 6 b,c), where stratigraphic unconformities are known to deepen eastward (Martelli
245 et al., 2017). At 2.5 s, the maximum amplification concentrates in the Adriatic zone, with values
246 between 1.5-2.5 that decrease to 1-1.5 in the rest of the basin (Figure 6d).
247 The variability of the amplification functions is shown in Figure 7 as difference between the 84^{th} and
248 50^{th} percentile of the frequency distribution of 1000 outcomes (100 randomizations times 10 input
249 motion) for each site. As for Figure 6, also the variability in the results presents an eastward increase
250 regardless of period, with maximum values that occur in different part of the basin depending on
251 period. At 1-1.25s, the maximum difference between the 84^{th} and 50^{th} percentile is about 0.3-0.4 in
252 an area northeast of Casaglia (Figure 7a,b), moving southward at 1.67 s (Figure 7c). The variability
253 increases at 2.5s, with values of 0.4-0.5 in the central plain (Figure 7d). For this period, most of the
254 study area presents differences between the 84^{th} and 50^{th} percentile greater than 0.3, with smaller
255 values south of Mirandola and Casaglia, and westward.
256
257 **Soil model testing**
258 To verify the accuracy of the seismo-stratigraphic model, the numerical results are compared with
259 the corresponding experimental counterpart at target sites. Usually, experimental amplification
260 functions are determined through the well-established Standard Spectral Ratio (SSR) method
261 (Borcherdt, 1970), which calculates the spectral ratio of earthquake recordings at a target site to the
262 recordings of the same earthquakes at a nearby reference site. As most recording sites in the Po Plain
263 are located on alluvial deposits, far away from a reference site, the SSR approach is inapplicable in
264 this study (e.g., Massa and Augliera 2013; Laurenzano et al., 2017). Hence, we consider recordings
265 of borehole stations located at depths corresponding to the base of our numerical model (i.e., seismic

bedrock depth in Figure 1). Table 1 lists the borehole stations considered, while their geographic distribution is shown in Figure 1. For each station, we select a set of events occurred between January 2012 and January 2019, with magnitude between 3.0 and 5.1 at a source-to-site distance up to 135 km. The main features of these events are listed in Table 2. Finally, we compute the surface-to-borehole Fourier spectral ratio as the ratio of the Fourier Amplitude Spectra (FAS) at the surface level to the FAS at the borehole level. This function does not strictly represent the site amplification, but allows verifying the consistency of the soil model down to the receiver depth in an effective way.

The processing of the data recorded at the target sites consists in:

- correction for the instrumental response (only in the case of velocimetric records) and trend;
- application of baseline and tapering correction;
- selection of *S*-wave time windows on horizontal components, for both the surface and borehole recordings;
- for each signal window, computation of the FAS smoothed by applying the Konno and Ohmachi (1998) algorithm with $b = 40$;
- computation of the mean surface-to-borehole Fourier spectral ratio by averaging the spectral ratios of the FASs of the surface recordings to the FASs of the corresponding borehole recordings.

The spectral ratios are computed considering frequencies with signal-to-noise ratio (SNR) larger than a threshold of 2. The two horizontal components are analyzed separately in order to detect possible directional effects.

At each site, the experimental surface-to-borehole Fourier spectral ratios are compared with the corresponding numerical functions, which are computed as the ratio of the FASs of the motions at the ground surface to the FASs of the input motions within the profile (at the base rock level). Figure

290 8 shows the comparison of the numerical and experimental surface-to-borehole Fourier spectral ratios
291 at MIRB (a), FERS (b), SERM (c), and CTL8 (d). On average, the simulations are in good agreement
292 with the experimental observations, particularly as concerns the shape of the interferometric curves
293 and the resonance frequencies of the sites. These are well reproduced at MIRB (Figure 8a), FERS
294 (Figure 8b), and SERM (Figure 8c). Some discrepancies can be observed in the amplitude values in
295 correspondence of the first resonance peak, where the mean numerical functions may exceed the
296 experimental curves (in particular at SERM). This effect is probably due to overestimation of the
297 seismic impedance contrast at the base of the models, where an average *Vs* of 800 m/s is set
298 throughout the Po Plain area. Nevertheless, the experimental curves at all these sites are well within
299 the uncertainty band indicated by the bundle of numerical curves (grey lines in Figure 8). CTL8
300 (Figure 8d) is the only site with directional effects, showing maximum amplitudes of 7.5 and 11.5 for
301 the E-W and N-S components, respectively. At this site, the mean numerical surface-to-borehole
302 Fourier spectral ratio is in good agreement with the experimental one corresponding to the N-S
303 component. Some discrepancies occur at long periods (> 2 s), where the numerical functions are well
304 below the experimental curves.

305

306 # Discussion: does the 1-D assumption hold for the Po Plain?

307 In this study, a 1-D approach was considered to evaluate the effects of the shallower soils (i.e., first
308 hundreds of meters) on surface ground motion. We deemed the 1-D approach acceptable for most the
309 Po Plain, as surface stratigraphy is typically characterized by horizontal layers of alluvial deposits
310 and lateral heterogeneities are supposed to be smooth at regional scale. Therefore, our numerical
311 analyses do not account for the generation of surface-waves, and the response of soil deposits is
312 assumed to be predominantly related to *SH*-waves propagating vertically from the underlying
313 bedrock. However, different numerical modelling (e.g. Vuan et al., 2011; Paolucci et al., 2015b; Klin
314 et al., 2019) and analysis of the recordings of the Emilia sequence (e.g., Luzi et al., 2013; Bordoni et

al., 2012) have highlighted that 2-D and 3-D effects can be significant due to the complex buried morphology of the basin. In these cases, our results might underestimate the amplitude and duration of the seismic motion, and, consequently, the amplification functions.

To investigate the possible limitations of 1-D ground response analysis, a further test is carried out at the same target sites considered in Figure 8. The surface response spectra obtained from the numerical analyses are normalized to the PGA value and compared to the normalized response spectra of the stronger ground motions recorded at the ground surface (Figure 9). The strong motion records are selected in order to be consistent with the magnitude-distance scenarios controlling the seismic hazard at the target sites (Barani et al., 2009). While the hazard at MIRB, FERS, and SERM is dominated by scenario events with source-to-site distances less than 60 km and magnitude less than 6, the hazard at CTL8 is controlled by distant scenarios (60 km < R < 120 km), again with magnitude between 4 and 6 (see Mascandola et al., 2020). At MIRB and FERS (Figure 9a and 9b), the average spectrum of strong motion recordings is in agreement with the one resulting from the equivalent linear simulations, indicating that the numerical results are consistent with the observed site effects. Similar observations hold for SERM (Figure 9c), for which the average response spectrum of the strong motion recordings is slightly above the one resulting from the equivalent linear analyses for 0.5 < T < 1 s and T > 1.5 s. The differences between the empirical and numerical response spectra increases at CTL8 (Figure 9d), where the average spectrum of the strong motion recordings is always above the one obtained from the numerical modeling. For this site, where the numerical soil model is available down to the geologic bedrock at 1300 m depth (Mascandola et al., 2017), we have investigated the influence of the deeper seismic impedance contrast between the geologic bedrock and the overlying deposits, by performing additional ground response analyses (Yamanaka et al., 2012 and Zhu et al., 2020). For this site, driving the input motion at the top of the geologic bedrock (so to consider the effect of the two main impedance contrasts in the soil profile, at the seismic and geologic bedrock depths) yields a better agreement, but still a good matching is not observed (Figure

9b). This suggests that 1-D numerical simulations at CTL8 are insufficient to exhaustively reproduce the observed ground motion for $T > 1$ s. As noted above, contrary to the other target sites, the strong motion data set considered for CTL8 is richer in distant events (compare the magnitude-distance distributions in the insets in Figure 9). Hence, 2-D (or 3-D) propagation effects can be invoked to explain the underestimation in the 1-D numerical results at CTL8, and possibly at other sites in the Po Plain. To verify this, we compare the numerical amplification functions with those provided by the ground motion prediction equation (GMPE) of Northern Italy (Lanzano et al. 2016), for soil categories C (i.e., $V_{S,30}$ between 180 and 360 m/s, European Committee for Standardization, 2004) and C1 (class C sites located within the Po Plain alluvial basin; Lanzano et al., 2016). The rationale behind class C1 is that complex 2-D and 3-D site effects are expected to occur due to the generation of surface waves at the basin edges, with remarkable soil amplification at frequencies smaller than 1 Hz. The selected GMPE is specifically calibrated for the Po Plain area and northeastern Italy, by taking advantage of the large number of recordings associated with the 2012 Emilia sequence. Thus, the related amplification function (i.e, site term for a specific soil class) represents an important benchmark, although it can be influenced by the strong motion data set used, which is mostly composed of recordings associated with a specific seismic sequence.

The comparison between our numerical amplification functions and those provided for soil category C indicates a good agreement (Figure 10a). On the other hand, some differences can be observed with the amplification curve for the C1 soil category, which presents higher amplifications between 2.5 and 3 in the long period range (i.e., T > 1s). In this case, our model may lead to underestimations up to about 60% (Figure 10a). The difference between the soil amplification function for the C1 and C classes is quantified by $\delta_{bas}(T)$ term in Lanzano et al. (2016). This corresponds to a basin-effect correction term that accounts for the generation of surface waves at the basin edges. Since our numerical modelling does not account for basin effects, we adjust our median amplification functions by adding the $\delta_{bas}(T)$ term, thus to obtain results comparable with the amplification curves for the C1

soil category (Figure 10b). As with Figure 10a, also Figure 10b shows that our numerical results follow at least two different trends, corresponding to different sectors of the Po Plain (Figure 10c). The former (dark grey in Figure 10) is peaked around 0.6-1.5 s and can be observed in most of the Po Plain area, in particular in the northwest sector (Figure 10c). The latter (light grey in Figure 10) presents a flat response for periods longer than 0.6 s, and can be observed in a more limited area, in the southeast sector of the Po Plain (Figure 10c). In this zone, the seismic bedrock is deeper (Figure 1) and the shear-wave velocities are lower (Figure 2) than the rest of the basin, inducing soil amplifications at longer periods (Mascandola et al., 2019). The regional GMPE considered here captures just one of these trends (light grey in Figure 10a and 10b), probably due to the uneven distribution of the recording stations in the strong-motion dataset (see Lanzano et al., 2016).

Conclusions

This work has presented a further effort towards the characterization of site effects in the Po Plain sedimentary basin, where many geological components contribute to the characteristics of the surface ground motion. While previous research mainly focused on the role of the deep structure of the basin on surface ground motion, here we have analyzed the contribution of the shallower deposits (i.e., first hundreds of meters), with focus on long-period ground motion (i.e., 1-3 s), where amplification effects due to the soft sediments above seismic bedrock were observed.

To this end, a regional shear-wave velocity model was defined by interpolation of selected shear-wave velocity (*Vs*) profiles from microtremor arrays and borehole tests, taking advantage of geophysical data recently acquired, and considering the deep seismic bedrock morphology defined in Mascandola et al. (2019). To perform extensive 1-D ground response analyses, the study area was discretized into a grid, and for each node, a discrete *Vs* profile was defined with a corresponding soil parametrization. The uncertainty was considered by randomly varying the values of the soil properties

via Monte Carlo simulations. For each grid node, a 1-D ground response analysis was performed by adopting an equivalent linear approach. To verify the consistency of the soil amplification model, the numerical results were compared with the corresponding experimental counterpart at target sites. In this regard, we considered a set of borehole seismic stations where recordings of the same set of earthquakes were available both at the surface and at the seismic bedrock depth. These comparisons proved the consistency of the 1-D numerical simulations, despite a possible overestimation of the seismic impedance contrast at the base of the model.

Finally, the 1-D assumption was tested by comparing numerical and empirical observations at the ground surface (in terms of normalized response spectra), and by comparing the numerical amplification functions with the empirical amplification curves provided by Lanzano et al. (2016). We found that 1-D ground response analyses may underestimate the actual site amplification, especially in far-field recordings dominated by surface waves. In this case, the median soil amplification model can lead to average underestimations of 30%, up to a maximum underestimation of 60%. To account for the generation of surface waves (i.e., 3-D basin effects), the 1-D amplification functions can be adjusted by simply adding the basin-effect correction term provided by Lanzano et al. (2016) for the Po Plain area. We found that the corrected amplification functions were comparable with the empirical observations, proving the accuracy of such a correction for future applications. Moreover, compared to the amplification functions provided by the region-specific ground motion prediction equation of Lanzano et al (2016), they were found to better represent the variability of the 1-D component in soil amplification.

These findings pose the problem of correctly incorporating site effects and handling their uncertainty in probabilistic seismic hazard analyses and risk assessments in the Po Plain area. Remarks of this work should be taken into account in future applications aimed at risk evaluation and mitigation in this region, such as seismic hazard analysis, seismic microzonation studies, and ground response analyses for building design.

Data and Resources

The seismic networks cited are the National Seismic Network (http://cnt.rm.ingv.it/en/instruments/network/IV), the Northeast Italy Seismic Network (http://rts.crs.inogs.it/) and the Italian Accelerometric Network (http://ran.protezionecivile.it/IT/index.php). The Geological Survey of the Emilia-Romagna Authority is available at https://ambiente.regione.emilia-romagna.it/it/geologia/servizio-geologico-sismico-e-dei-suoli. The M_W 5.8 20 May 2012 earthquake is available at http://terremoti.ingv.it/. All web sites were last accessed on February 04, 2021. The list of acceleration time histories, considered in the present study for the ground response analyses, is available in the Electronic Supplement.

Acknowledgments

This study is part of a Ph.D. thesis at the University of Pisa, Italy. This study has also benefited from funding provided by the Italian Presidenza del Consiglio dei Ministri–Dipartimento della Protezione Civile (DPC)—Agreement B2, DPC-INGV. This paper does not necessarily represent DPC official opinions and policies.

We are thankful to Prof. Roberto Paolucci for the precious suggestions that improved the critical discussion of the 1-D ground response results. We would also express our gratitude to Giovanni Lanzano and Francesca Pacor for their feedback and for providing us with the available within-event ground motion residuals.

References

Barani, S., D. Albarello, D. Spallarossa, and M. Massa (2015). On the influence of horizontal ground-shaking definition on probabilistic seismic hazard analysis. Bull. Seism. Soc. Am. 105(5), 2704-2712.

Barani, S., R. De Ferrari, and G. Ferretti (2013). Influence of soil modeling uncertainties on site response. Earthquake Spectra 29(3), 705-732.

Barani, S., D. Spallarossa, and P. Bazzurro (2009). Disaggregation of probabilistic ground-motion hazard in Italy, Bull. Seismol. Soc. Am., 99(5), 2638-2661.

Bazzurro, P., and C.A. Cornell (2004). Ground-motion amplification in nonlinear soil sites with uncertain properties, Bull. Seismol. Soc. Am., 94(6), 2090-2109.

Borcherdt, R.D. (1970). Effects of local geology on ground motion near San Francisco Bay. Bull. Seismol. Soc. Am. 60:29–61.

Bordoni, P., F. Pacor, G. Cultrera, M. Massa, P. Casale, F. Cara, G. Di Giulio, D. Famiani, C. Ladina, M. Pischiutta, M. Quintiliani, G. Milana, A. Mercuri, C. Marcocci, V. Pessina, E. D'Alema, S. Lovati, C. Mascandola, M. D'Amico, C. Felicetta, L. Luzi, R. Puglia, A. Fodarella, S. Pucillo, R. Cogliano, G. Riccio, L. Zarrilli, L. Scarfi, R. Azzaro, S. Branca, S. Di Prima, G. Tusa, L. Zuccarello, M. Paratore, A. Scaltrito, D. Di Naccio, S. Amoroso, G. Di Giulio, L. Cantore, M. Vassallo, and M. Cattaneo (2017). Caratterizzazione sismica delle stazioni accelerometriche italiane nell'ambito della Convenzione DPC-INGV 2016-17, Allegato B2 Obiettivo 1 Task B, Atti del 36° Convegno Annuale del GNGTS, 228-230 (in Italian).

Bordoni, P., R. M. Azzara, F. Cara, R. Cogliano, G. Cultrera, G. Di Giulio, A. Fodarella, G. Milana, S. Pucillo, G. Riccio, A. Rovelli, P. Augliera, L. Luzi, S. Lovati, M. Massa, F. Pacor, R. Puglia, and G. Ameri (2012). Preliminary results from EMERSITO, the rapid response network for site effect studies. Annals of Geophysics.

459 Burrato, P., F. Ciucci, and G. Valensise (2003). An inventory of river anomalies in the Po Plain,
460 Northern Italy: evidence for active blind thrust faulting. Annals of Geophysics, 46(5).

461 Davis, P. M., J.L. Rubinstein, K.H. Liu, S.S. Gao, and L. Knopoff (2000). Northridge earthquake
462 damage caused by geologic focusing of seismic waves. Science, 289(5485), 1746-1750.

463 EPRI. (1993). Guidelines for Determining Design Ground Motions. EPRI TR-102293.

464 European Committee for Standardization (2004). Eurocode 8: design of structures for earthquake
465 resistance. P1: General rules, seismic actions and rules for buildings. Draft 6, Doc
466 CEN/TC250/SC8/N335.

467 Furumura, T., and Kennett, B. L. N. (1998). On the nature of regional seismic phases—III. The
468 influence of crustal heterogeneity on the wavefield for subduction earthquakes: the 1985 Michoacan
469 and 1995 Copala, Guerrero, Mexico earthquakes. Geophysical Journal International, 135(3), 1060-
470 1084.

471 GeoMol Team (2015). GeoMol - Assessing subsurface potentials of the Alpine Foreland Basins for
472 sustainable planning and use of natural resources - Project Report, 188 pp. (Augsburg, LfU).

473 Grazier, V., A. Shakal, C. Scrivner, E. Hauksson, J. Polet, and L. Jones (2002). TriNet strong-motion
474 data from the M 7.1 Hector Mine, California , earthquake of 16 October 1999, Bull. Seismol. Soc.Am.
475 92, 1525–1542.

476 Idriss, I. M. (2011). Use of Vs30 to represent local site conditions, in 4th LASPEI/IAEE International
477 Symposium Effects of Surface Geology on Strong Ground Motions, Santa Barbara, CA.

478 Idriss, I. M., and J. I. Sun (1992). User's manual for Shake91: A computer program for conducting
479 equivalent linear seismic response analyses of horizontally layered soil deposits, Center for
480 Geotechnical Modelling, Department of Civil and Environmental Engineering, University of
481 California, Davis.

Kaklamanos, J., L. G. Baise, E. M. Thompson, and L. Dorfmann (2015). Comparison of 1D linear, equivalent-linear, and nonlinear site response models at six KiK-net validation sites. Soil Dynamics and Earthquake Engineering, 69, 207-219.

Kaklamanos J., B. A. Bradley, E. M. Thompson, and L. G. Baise (2013). Critical parameters affecting bias and variability in site-response analyses using KiK-net downhole array data, Bull. Seismol. Soc. Am., 103(3): 1733-1749.

Kim, B., Hashash, Y., Stewart, J.P., Rathje, E.M., Harmon, J.A., Musgrove, M.I., Campbell, K.W., and Silva, W.J. (2016). Relative Differences between Nonlinear and Equivalent-Linear 1D Site Response Analyses. Earthquake Spectra, 32, 1845-1865.

Klin, P., G. Laurenzano, M.A. Romano, E. Priolo, and L. Martelli (2019). ER3D: a structural and geophysical 3-D model of central Emilia-Romagna (northern Italy) for numerical simulation of earthquake ground motion. Solid Earth, 10(3), 931-949.

Koketsu, K. M., and H. Miyake (2008). A seismological overview of long-period ground motion, J. Seismol. 12, 133–143.

Lanzano, G., M. D'Amico, C. Felicetta, R. Puglia, L. Luzi, F. Pacor, and D. Bindi (2016). Ground-motion prediction equations for region- specific probabilistic seismic- hazard analysis, Bulletin of the Seismological Society of America, 106(1), 73-92.

Laurenzano, G., E. Priolo, M. Mucciarelli, L. Martelli, and M. Romanelli (2017). Site response estimation at Mirandola by virtual reference station, Bull. Earthq. Eng., 15(6), 2393-2409.

Luzi, L., F. Pacor, G. Ameri, R. Puglia, P. Burrato, M. Massa, P. Augliera, G. Franceschina, S. Lovati, and R. Castro (2013). Overview on the strong motion data recorded during the May–June 2012 Emilia seismic sequence, Seismol. Res. Lett. 84, no. 4, 629–644.

Martelli, L., M. Bonini, L. Calabrese, G. Corti, G. Ercolessi, F. C. Molinari, L. Piccardi, S. Pondrelli, F. Sani, and P. Severi (2017). Carta sismotettonica della Regione Emilia-Romagna e aree limitrofe,

scala 1:250.000 (edizione 2016). Con note illustrative, Regione Emilia-Romagna, SGSS; CNR, IGG sez. FI; Università degli Studi di Firenze, DST; INGV sez. BO. D.R.E.AM. Italia (in Italian).

Martelli, L., and M. Romani (2013). Microzonazione Sismica e analisi della condizione limite per l'emergenza delle aree epicentrali dei terremoti della pianura emiliana di maggio-giugno 2012, relazione illustrativa, Servizio geologico, sismico e dei suoli Regione Emilia Romagna (in Italian).

Mascandola, C., Barani, S., Massa, M., Paolucci, E., and Albarello, D. (2020). Clustering analysis of probabilistic seismic hazard for the selection of ground motion time histories in vast areas. Bulletin of Earthquake Engineering, 1-20.

Mascandola, C., M. Massa, S. Barani, D. Albarello, S. Lovati, L. Martelli, and V. Poggi (2019). Mapping the Seismic Bedrock of the Po Plain (Italy) through Ambient- Vibration Monitoring, Bull. Seismol. Soc. Am., 109(1), 164-177.

Mascandola, C., M. Massa, S. Barani, S. Lovati, and M. Santulin (2017). Long- Period Amplification in Deep Alluvial Basins and Consequences for Site- Specific Probabilistic Seismic- Hazard Analysis: An Example from the Po Plain (Northern Italy), Bull. Seismol. Soc. Am., 107(2), 770-786.

Massa, M., and P. Augliera (2013). Teleseisms as estimator of experimental long period site amplifications: Example in the Po Plain (Italy) from the 2011 Mw 9.0 Tohoku-Oki (Japan) earthquake, Bull. Seismol. Soc. Am. 103, no. 5, 2541–2556.

Mayne, P.W. (2001). Stress-strain-strength-flow parameters from seismic cone tests. Intl. Conf. on In-Situ Measurement of Soil Properties & Case Histories, Bali, Indonesia, 27-48.

Milana, G., P. Bordoni, F. Cara, G. Di Giulio, S. Hailemikael, and A. Rovelli (2013). One-dimensional velocity structure of the Po River plain (northern Italy) assessed by combining strong motion and ambient noise data, Bull. Earthq. Eng. 12, no. 5, 2195–2209.

528 Ministero delle Infrastrutture e dei Trasporti (2018). Norme Tecniche delle Costruzioni. Part 3.2.2:
529 Categorie di sottosuolo e condizioni topografiche, Gazzetta Ufficiale n. 42 del 20 febbraio 2018 (in
530 Italian).

531 Miyazaki, S. I., Segall, P., Fukuda, J., and Kato, T. (2004). Space time distribution of afterslip
532 following the 2003 Tokachi- oki earthquake: Implications for variations in fault zone frictional
533 properties. Geophysical Research Letters, 31(6).

534 Molinari, I., A. Argnani, A. Morelli, and P. Basini (2015). Development and testing of a 3-D seismic
535 velocity model of the Po Plain sedimentary basin, Italy. Bulletin of the Seismological Society of
536 America, 105(2A), 753-764.

537 Muttoni, G., C. Carcano, E. Garzanti, M. Ghielmi, A. Piccin, R. Pini, S. Rogledi, and D. Sciunnach
538 (2003). Onset of major Pleistocene glaciations in the Alps, Geology, 31(11): 989-992.

539 Paolucci, E., D. Albarello, S. D'Amico, E. Lunedei, L. Martelli, M. Mucciarelli, and D. Pileggi
540 (2015a). A large scale ambient vibration survey in the area damaged by May–June 2012 seismic
541 sequence in Emilia Romagna, Italy, Bull. Earthq. Eng., 13(11), 3187-3206.

542 Paolucci, R., I. Mazzieri, and C. Smerzini (2015b). Anatomy of strong ground motion: near source
543 records and three-dimensional physics-based numerical simulations of the Mw 6.0 2012 May 29 Po
544 Plain earthquake, Italy, Geophys. J. Int., 203, 2001–2020.

545 Parolai, S. (2012). Investigation of site response in urban areas by using earthquake data and seismic
546 noise, New manual of seismological observatory practice, 2: 1-38.

547 Priolo, E., M. Romanelli, C. Barnaba, M. Mucciarelli, G. Laurenzano, L. Dall'Olio, N.A. Zeid, R.
548 Caputo, G. Santarato, L. Vignola, C. Lizza, and P. Di Bartolomeo (2012). The Ferrara thrust
549 earthquakes of May–June 2012: Preliminary site response analysis at the sites of the OGS temporary
550 network, Ann. Geophy. 55, no. 4, 591–597, doi: 10.4401/ag-6172.

551 Ratchkovski, N. A., R. A. Hansen, J. C. Stachnik, T. Cox, O. Fox, L. Rao, E. Clark, M. Lafevers, S.
552 Estes, J. B. MacCormack, and T. Williams (2003). Aftershock sequence of the Mw 7.9 Denali fault,
553 Alaska, earthquake of 3 November 2002 from regional seismic network data. Seismological Research
554 Letters, 74(6), 743-752.

555 Regione Emilia-Romagna, ENI – AGIP (1998). Riserve idriche sotterranee della Regione Emilia-
556 Romagna, a cura di G. Di Dio. S.EL.CA., Firenze (in Italian).

557 Regione Lombardia, Eni Divisione Agip (2002). Geologia degli acquiferi Padani della Regione
558 Lombardia, a cura di Cipriano Carcano e Andrea Piccin. S.EL.CA., Firenze (in Italian).

559 Scardia, G., R. De Franco, G. Muttoni, S. Rogledi, G. Caielli, C. Carcano, D. Sciunnach, and A.
560 Piccin (2012). Stratigraphic evidence of a Middle Pleistocene climate- driven flexural uplift in the
561 Alps, Tectonics, 31(6).

562 Schnabel, P.B. (1973). Effects of local geology and distance from source on earthquake ground
563 motions, PhD Dissertation, Univ. of California, Berkeley.

564 Tarabusi, G., and R. Caputo (2017). The use of H/V measurements for investigating buried tectonic
565 structures: the Mirandola anticline, Northern Italy, as a case study, Int. J. Earth. Sci., 106(1), 341-
566 353.

567 Toscani, G., P. Burrato, D. Di Bucci, S. Seno, and G. Valensise (2009). Plio-Quaternary tectonic
568 evolution of the Northern Apennines thrust fronts (Bologna-Ferrara section, Italy): seismotectonic
569 implications. Italian Journal of Geosciences, 128(2), 605-613.

570 Vuan, A., P. Klin, G. Laurenzano, and E. Priolo (2011). Far-source long period displacement
571 response spectra in the Po and Venetian Plains (Italy) from 3-D wavefield simulations, Bull. Seismol.
572 Soc. Am. 101, no. 3, 1055–1072.

573 Yamanaka, H., K. Chimoto, S. Tsuno, Y. P. Dhakal, M. Amrouche, N. Yamada, S. Fukumoto, and
574 K. Eto (2012). Estimation of S-Wave Velocity Profiles and Site Amplification Around the K-NET

Tsukidate Station, Miyagi Prefecture, with Reference to Large PGA During the 2011 off Pacific Coast of Tohoku Earthquake, Japan, J. Disaster Res.7, 682-692.

Zalachoris, G., and E. Rathje (2015). Evaluation of one-dimensional site response techniques using borehole arrays, Journal of Geotechnical and Geoenvironmental Engineering 141(12), 04015053.

Zhu, C., M. Pilz, and F. Cotton (2020). Evaluation of a novel application of earthquake HVSR in site-specific amplification estimation. Soil Dynamics and Earthquake Engineering, 139, 106301.

Claudia Mascandola

Marco Massa

Istituto Nazionale di Geofisica e Vulcanologia (INGV)

Via Alfonso Corti 12,

20133 Milano, Italy

claudia.mascandola@ingv.it (C.M.)

marco.massa@ingv.it (M.M.)

Simone Barani

Università degli Studi di Genova,

Dipartimento di Scienze della Terra, dell'Ambiente e della Vita,

Viale Benedetto XV 5,

16132 Genova, Italy

simone.barani@unige.it (S.B.)

Dario Albarello

Università degli Studi di Siena,

Dipartimento di scienze fisiche, della terra e dell'ambiente,

Via Laterina, 8

53100 Siena, Italy

dario.albarello@unisi.it (D.A.)

632 **List of Figure Captions**

633 **Figure 1:** Study area delimited by a white dashed line. The seismic bedrock depth provided by Mascandola et
634 al. (2019) is reported in meters from ground surface. White dots: distribution of selected *Vs* profiles for the
635 seismo-stratigraphic model. Black triangles: borehole seismic stations considered for the soil model testing
636 (Table 1).

637 **Figure 2:** a) Shear-wave velocity model of the Po Plain sedimentary basin down to the seismic bedrock depth
638 (Mascandola et al., 2019). The *Vs* classification is reported according to the Eurocode 8 (European Committee
639 for Standardization, 2004). The isobaths in correspondence of 180 m/s and 360 m/s are shown in panel b) and
640 c), respectively. Depths are in meters from the ground surface. The color version of this figure is available in
641 the electronic edition.

642

643 **Figure 3:** a) plan view of the 3-D seismic velocity model developed here and those of Klin et al. (2019),
644 Molinari et al. (2015), Paolucci et al. (2015b), and GeoMol Team (2015). Except for the GeoMol model (which
645 does not provide information about the distribution of seismic velocities at depth), the cross-sections (A-A'),
646 displayed in panels b), c), d), and e), show the distribution of *Vs* for each model mentioned above. b) This
647 study; c) Klin et al. (2019); d) Molinari et al. (2015); e) Paolucci et al. (2015b). The color version of this figure
648 is available in the electronic edition.

649 **Figure 4:** One hundred samples of randomized soil properties for a node of the study area (grey lines). Average
650 profiles are superimposed (black lines).

651 **Figure 5:** Variability of shear modulus reduction and damping curves. Average curves for soil deposits (EPRI,
652 1993) and bedrock (Schnabel, 1973) are superimposed (black lines). The curves associated with soil deposits
653 are for different depth ranges according to EPRI (1993). The arrows indicate the direction of increasing depth
654 in the soil profile (i.e., the darker the curves, the greater the depth). The depth ranges of the EPRI curves are:
655 6-15 m, 15-36 m, 36-76 m, 76-152 m, and 152-304 m.

Figure 6: Geographical distribution of the median amplification function, *AF(f)* at 1 s (a), 1.25 s (b), 1.67 s (c), and 2.5 s (c). The active tectonic structures are reported (Martelli et al., 2017), along with the locality of San Colombano, Mirandola and Casaglia that are in correspondence to the top of the main anticlines (i.e., buried ridges) of the study area. The color version of this figure is available in the electronic edition.

Figure 7: Difference between the 84^{th} and 50^{th} percentile of the distribution of amplification functions obtained from random simulations at 1s (a), 1.25s (b), 1.67s (c), and 2.5s (d). The active tectonic structures are reported (Martelli et al., 2017), along with the locality of San Colombano, Mirandola and Casaglia that are in correspondence to the top of the main anticlines (i.e., buried ridges) of the study area. The color version of this figure is available in the electronic edition.

Figure 8: Comparison between experimental and numerical surface-to-borehole Fourier spectral ratios at MIRB (a), FERS (b), SERM (c), and CTL8 (d). Grey curves: numerical functions associated with 1000 Monte Carlo realizations. Black solid curve: mean numerical function. Black dashed and dotted curves: mean experimental functions corresponding to the N-S and E-W components, respectively.

Figure 9: Comparison between the response spectra from numerical analyses (normalized to the PGA value) and those associated with the stronger ground motions recorded at MIRB a), FERS b), SERM c), and CTL8 d). The average response spectra resulting from the equivalent linear ground response analyses are displayed by black dashed lines. For CTL8, ground response results obtained by driving the seismic excitation at the top of the geologic bedrock is also shown (dotted-dashed line). The average response spectra of the strong motion records are displayed by black solid lines. The insets in the top right corner of each panel show the magnitude – distance distributions of the seismic events selected.

Figure 10: a) comparison between the numerical amplification functions *AF(T)* (grey curves) and those provided by the ground motion prediction equation of Northern Italy (Lanzano et al. 2016) for soil categories C (black solid line) and C1 (black dashed line). The latter identifies class C sites located within the Po Plain alluvial basin. b) The numerical amplification functions are corrected for the $\delta_{bas}(T)$ term provided by Lanzano et al. (2016) to account for 3-D basin effects. The shades of gray on both panel a) and b) highlight two different

trends in the amplification curves, whose spatial distribution is shown in panel c), along with the active tectonic structures (Martelli et al., 2017).

Table 1: Seismic stations considered for the computation of the empirical surface-to-borehole Fourier spectral ratios. Sens.1 is the seismic sensor at the surface; Sens. 2 is the seismic sensor in the borehole; Depth 2 is its corresponding depth in meters from ground surface IV: Italian National Seismic Network; OX: North-East Italy Seismic Network (see Data and Resources).

Network	Station	Locality	Lat. [°]	Lon. [°]	Sens. 1	Sens. 2	Depth 2 [m]
IV	CTL8	Castelleone	45.276	9.762	EpiSensor ±2g	Malin S-2	162
IV-OX	FERS-FERB	Casaglia	44.901	11.540	EpiSensor ±2g	Guralp CMG3T	130
IV	SERM	Sermide	45.010	11.296	EpiSensor ±2g	Lennartz 1s	135
OX	MIRB	Mirandola	44.878	11.063	Sara Force	Sara Force	126

Table 2: List of events used for the computation of the empirical surface-to-borehole Fourier spectral ratios.

Date and Time (UTC)	Lat. [°]	Lon. [°]	M_L	R_{epi}	station
25/01/2012 17:43:36	44.870	10.510	3.5	74	CTL8
23/12/2013 03:17:10	45.490	10.110	3.2	36	CTL8
21/11/2013 10:36:49	44.910	9.040	3.8	69	CTL8
22/11/2013 19:50:24	44.910	9.050	3.7	69	CTL8
24/01/2012 23:54:46	45.530	10.990	4.2	99	CTL8
03/06/2012 19:20:43	44.890	10.950	5.1	102	CTL8
12/06/2012 01:48:36	44.890	10.920	4.3	99	CTL8
03/10/2012 14:41:28	44.780	9.670	4.5	59	CTL8
25/01/2013 14:48:18	44.160	10.450	4.8	135	CTL8
24/03/2013 03:08:02	44.910	11.270	3.0	21	FERS-FERB
04/05/2013 05:11:06	44.870	11.520	3.8	9	FERS-FERB
14/06/2013 18:22:22	44.280	11.050	3.7	84	FERS-FERB

18/06/2013 20:25:10	45.540	10.980	3.0	83	FERS-FERB
04/09/2013 07:03:02	44.900	11.260	3.3	20	FERS-FERB
06/09/2013 01:45:08	44.890	11.280	3.4	20	FERS-FERB
20/10/2015 10:35:50	44.900	11.110	3.5	34	FERS-FERB
28/05/2016 03:31:40	44.920	11.290	3.1	20	MIRB
09/12/2016 07:21:50	44.330	10.480	3.9	80	MIRB
22/12/2016 01:34:38	45.010	11.340	3.0	25	MIRB
20/06/2017 01:37:12	44.200	11.520	3.7	95	MIRB
09/09/2017 18:12:29	44.620	11.940	3.0	95	MIRB
19/11/2017 12:37:44	44.660	10.030	4.4	90	MIRB
19/11/2017 12:10:12	44.670	10.040	3.3	90	MIRB
07/04/2016 18:25:56	44.650	12.070	3.2	83	MIRB
04/07/2016 11:37:22	44.930	11.290	3.5	15	MIRB
20/10/2015 10:35:50	44.900	11.110	3.5	20	SERM
19/11/2017 12:37:44	44.660	10.030	4.4	104	SERM
20/06/2017 01:37:12	44.200	11.520	3.7	95	SERM
04/07/2016 11:37:22	44.930	11.290	3.5	11	SERM
09/12/2016 07:21:50	44.330	10.480	3.9	98	SERM
28/05/2016 03:31:40	44.920	11.290	3.1	9	SERM
19/11/2017 12:37:44	44.660	10.030	4.4	104	SERM
14/01/2019 23:03:57	44.350	12.290	4.3	108	SERM

691

Figure1

Click here to access/download;Figure;Fig1.jpg

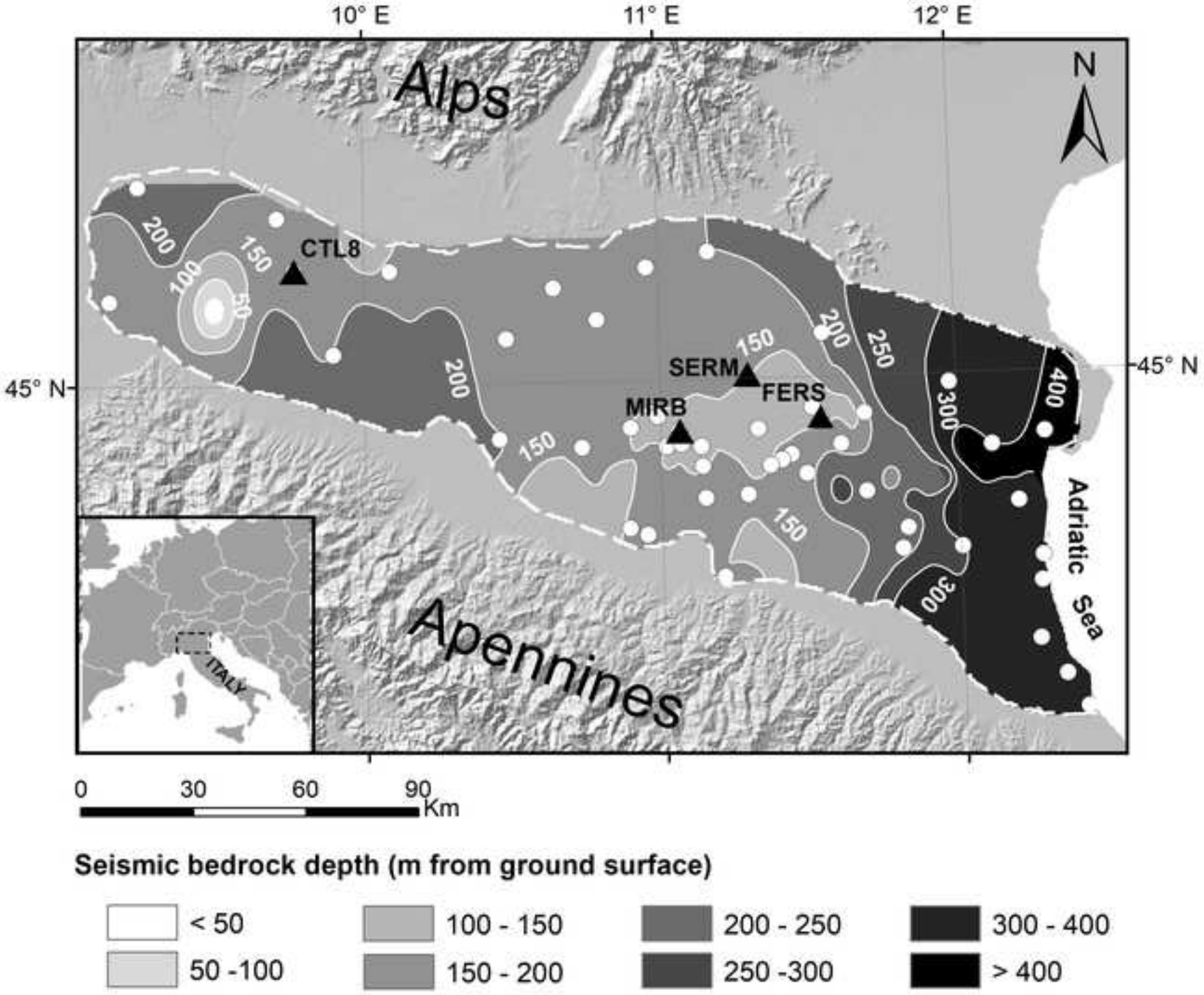

Figure2

Click here to access/download;Figure;Fig2.jpg

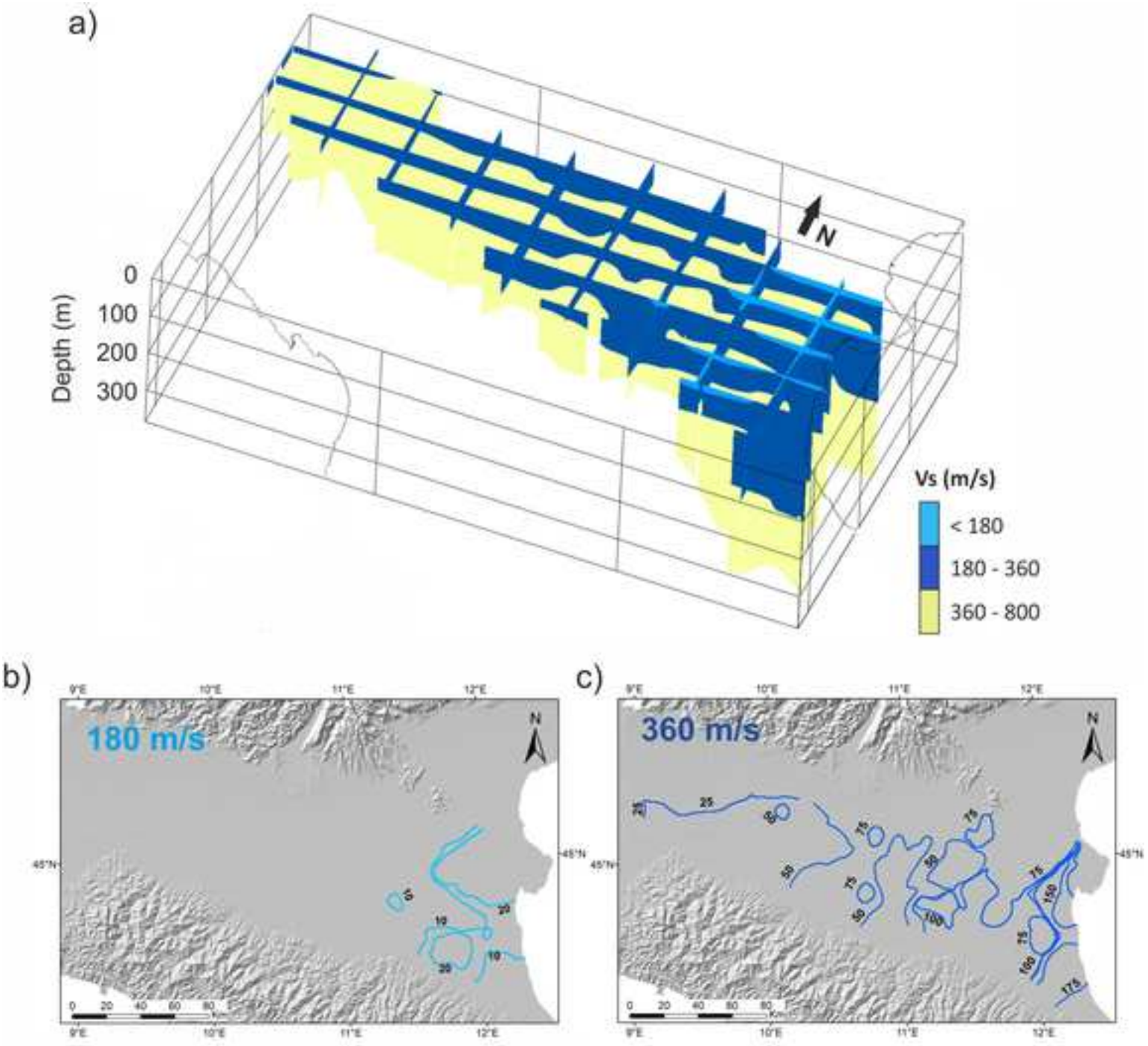

Figure3

Click here to access/download;Figure;Fig3.jpg

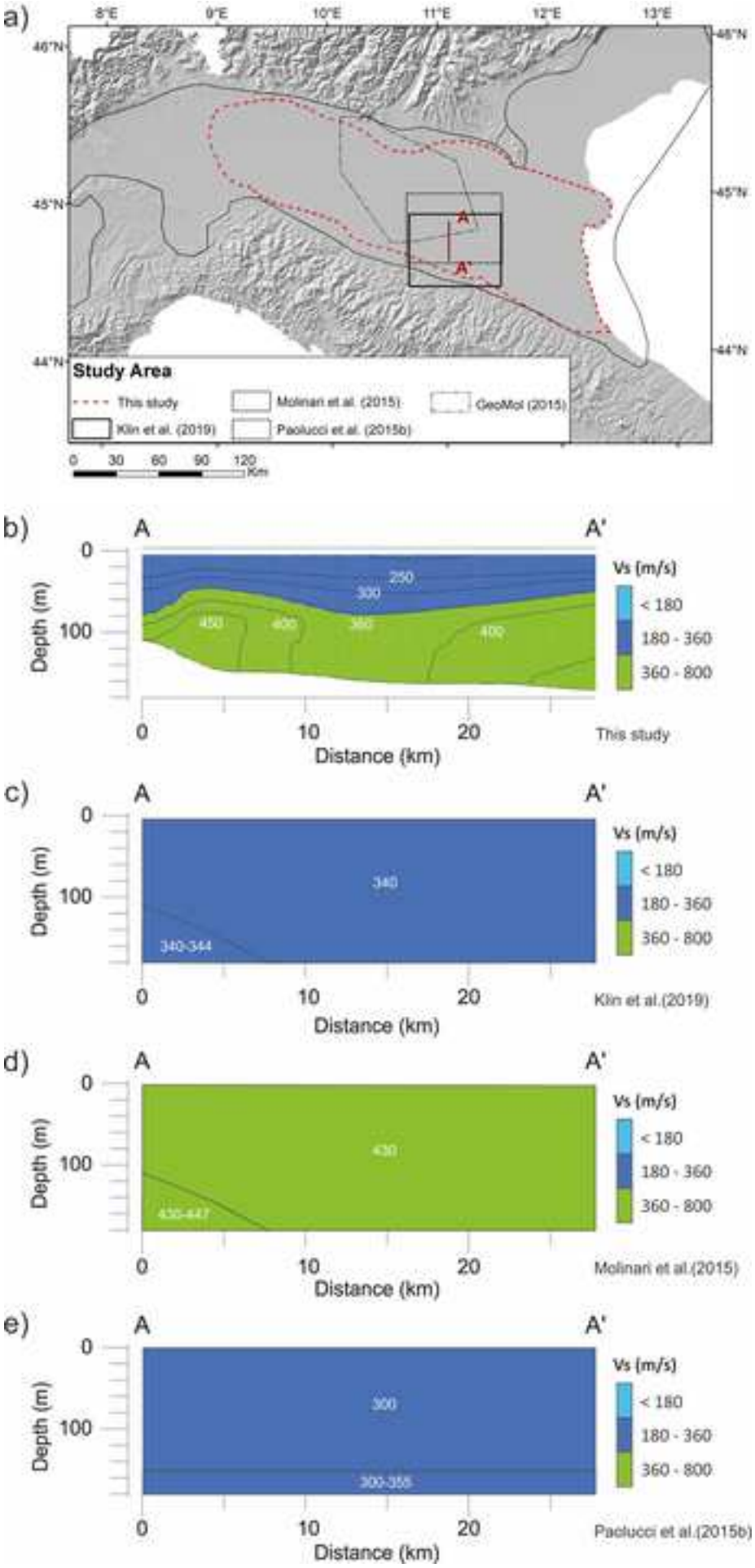

Figure4

Click here to access/download;Figure;Fig4.jpg

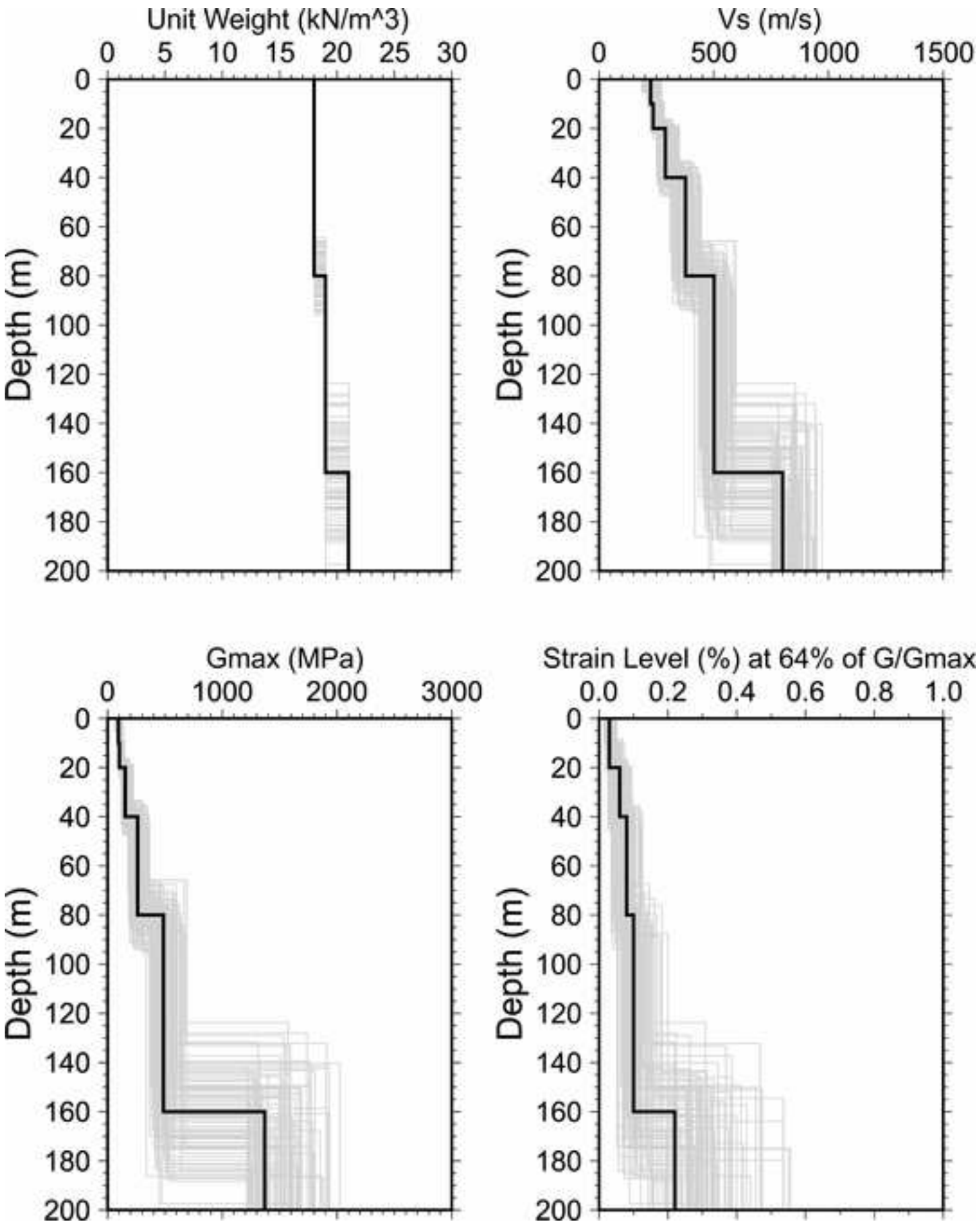

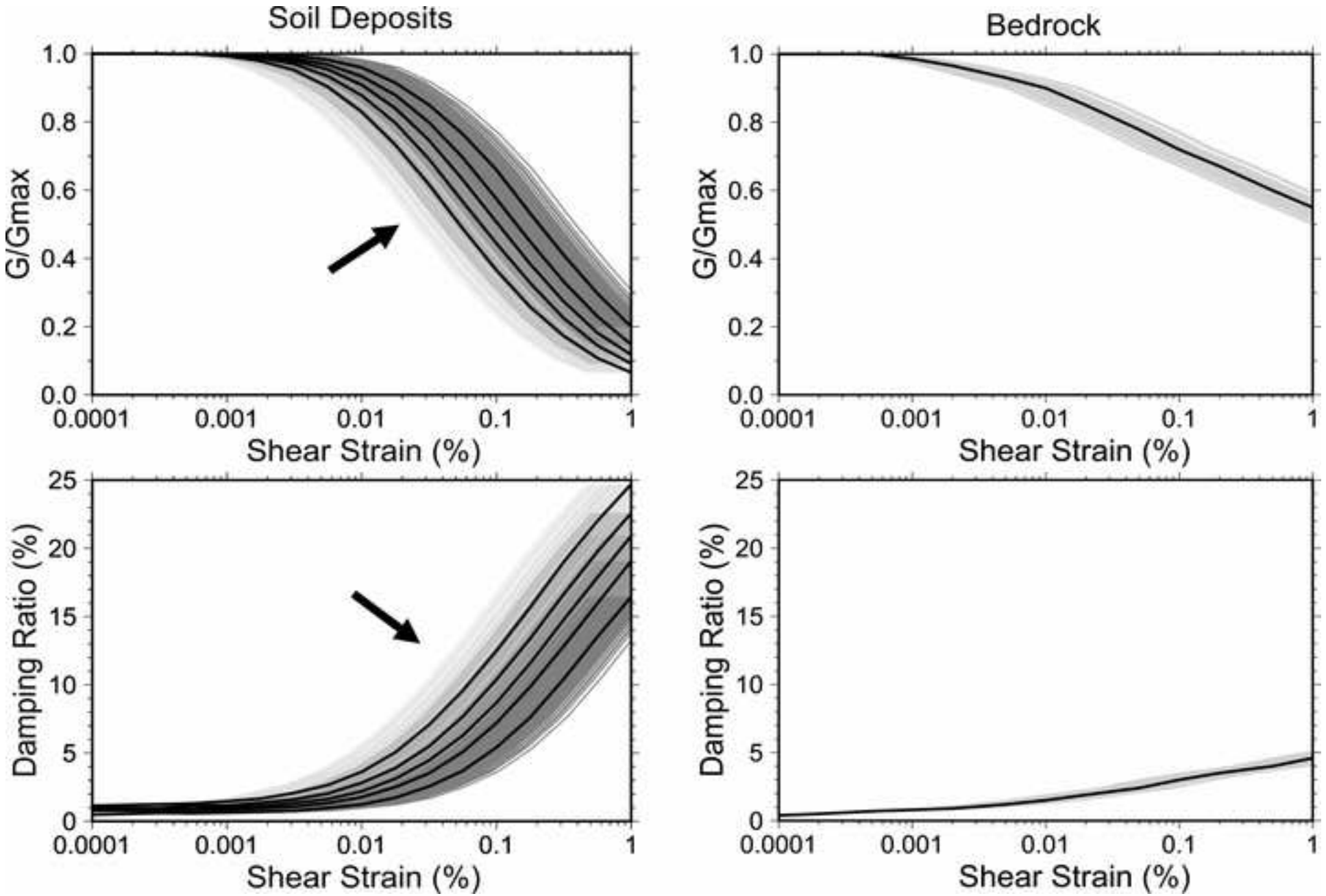

Figure6

Click here to access/download;Figure;Fig6.jpg

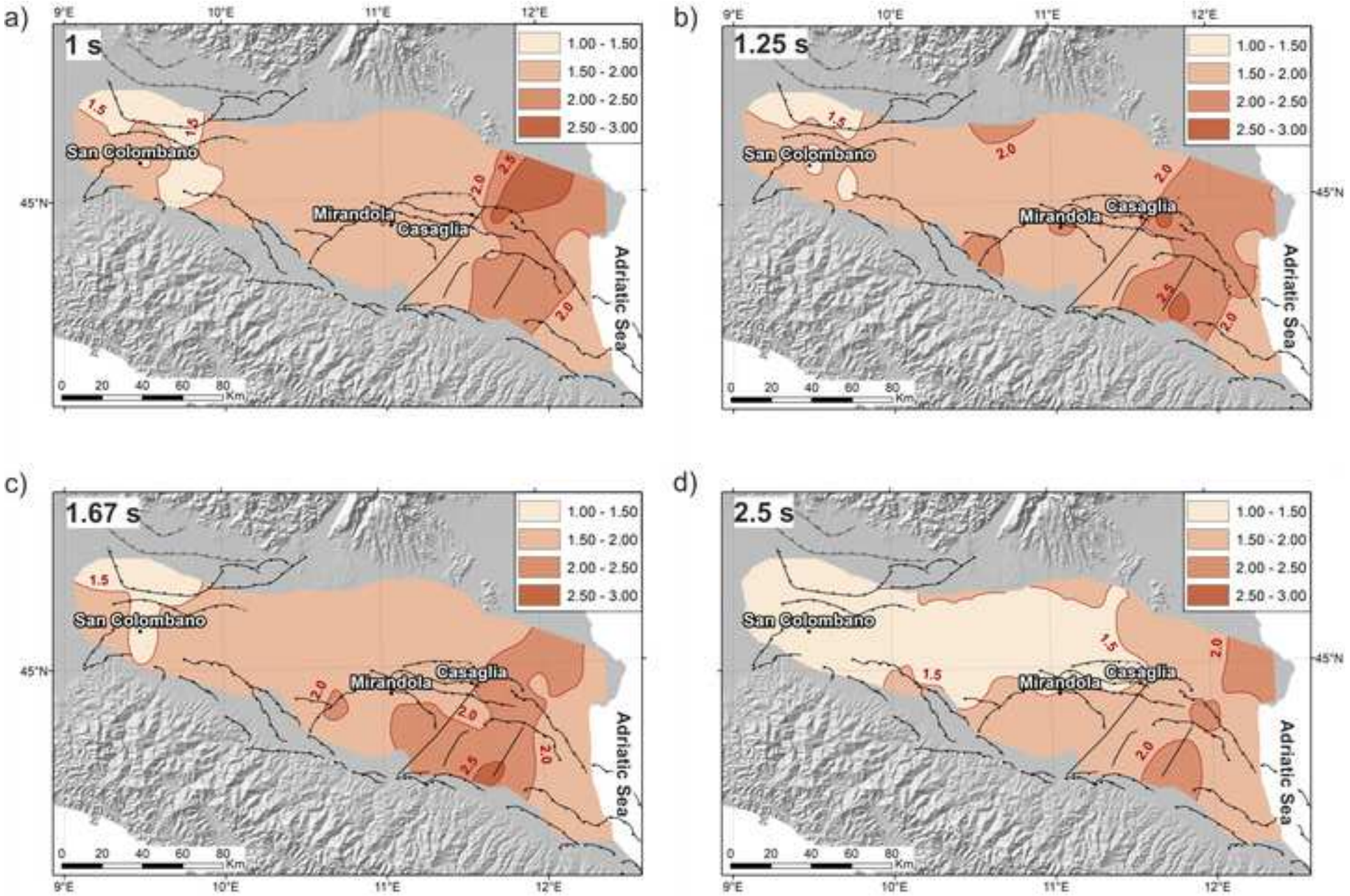

Figure7

Click here to access/download;Figure;Fig7.jpg

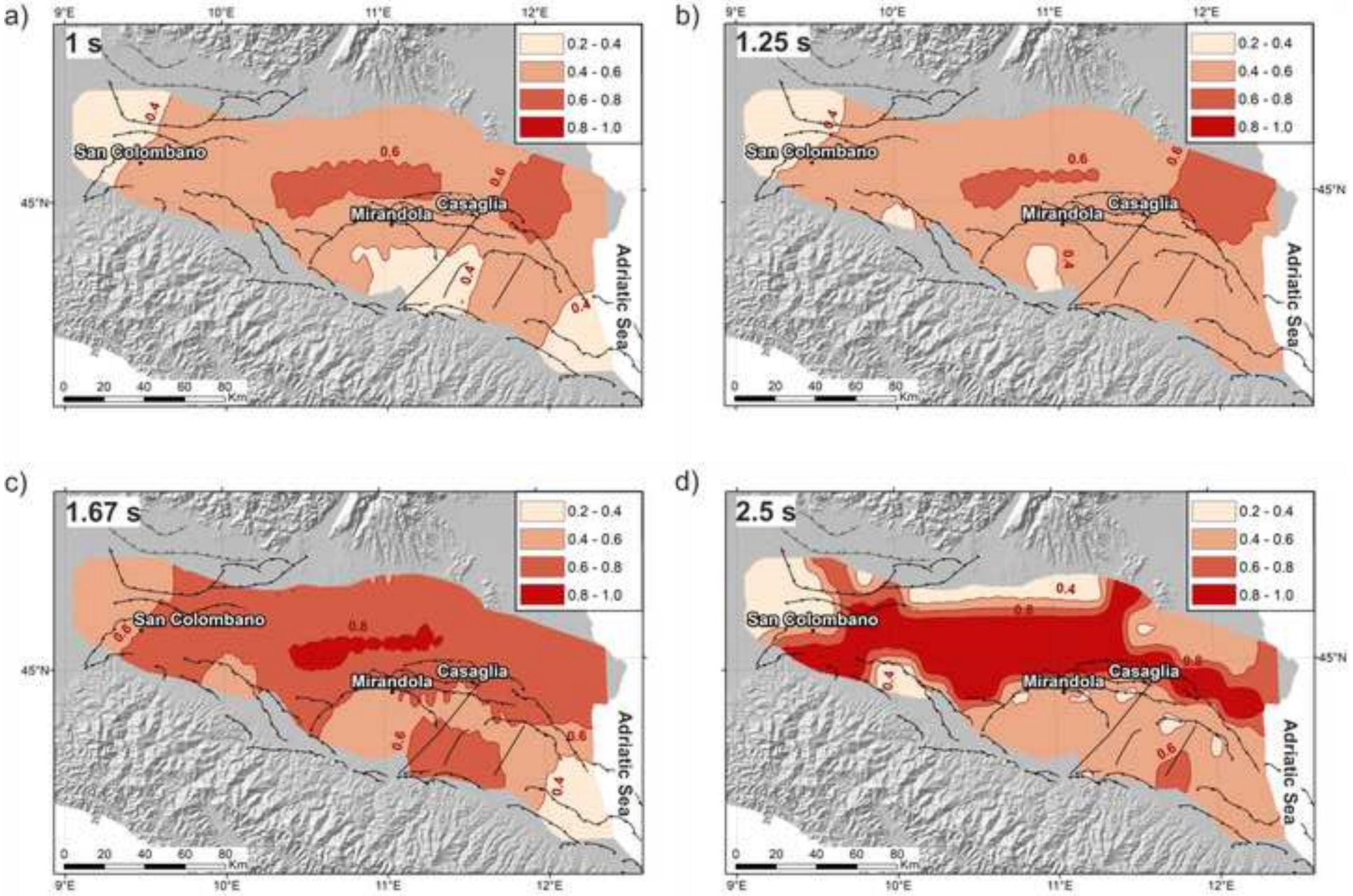

Figure8

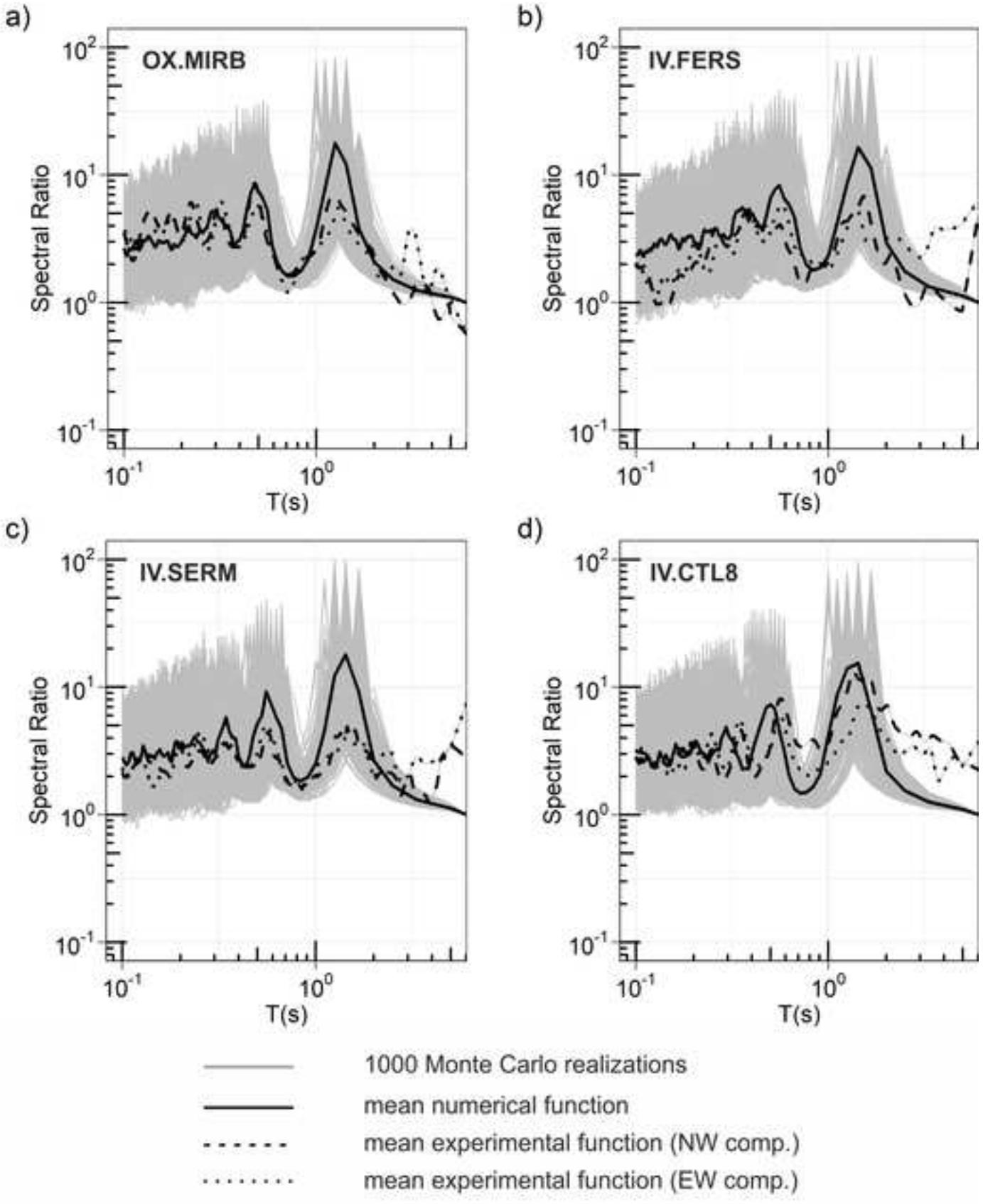

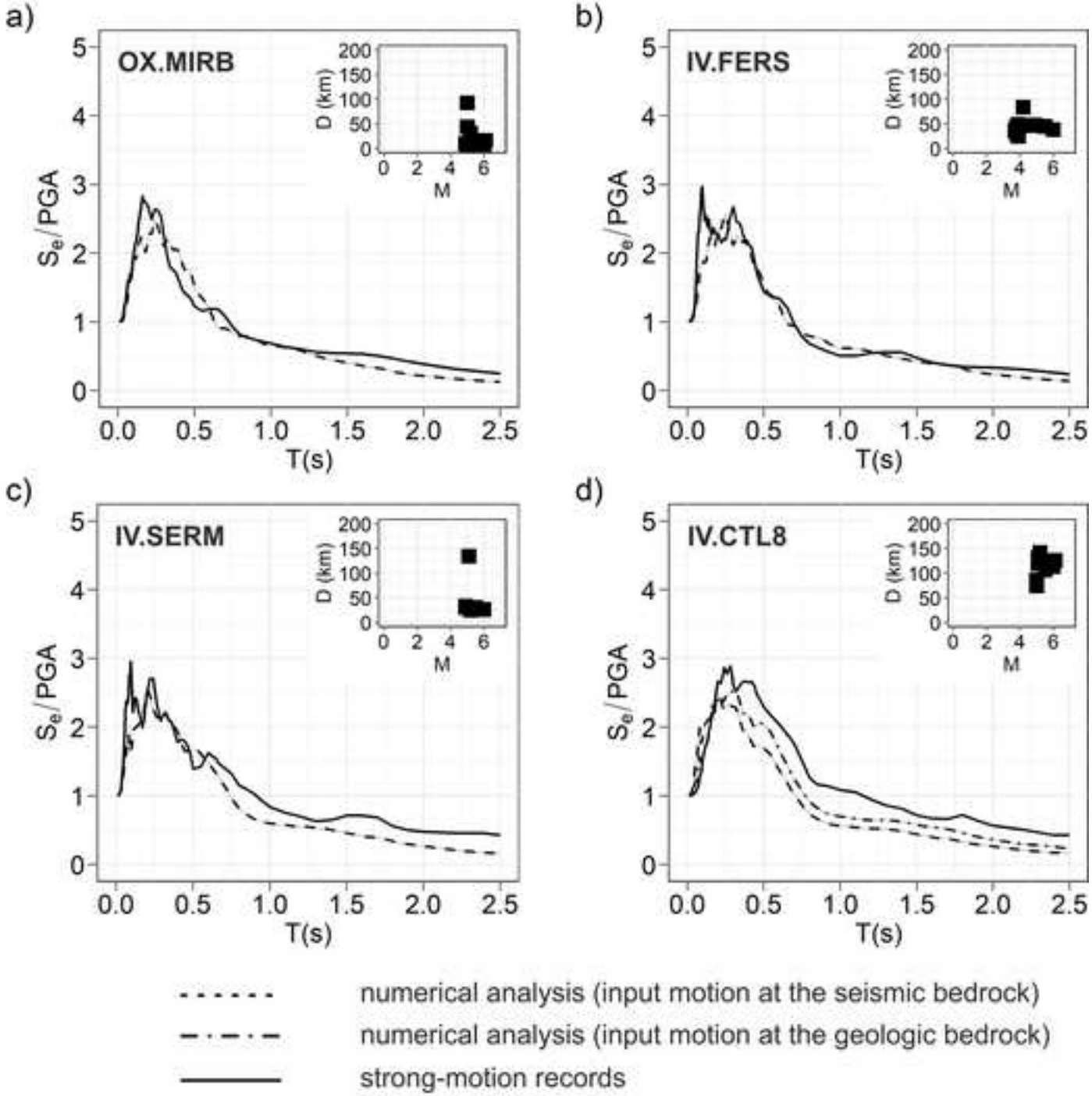

Figure10

Click here to access/download;Figure;Fig10.jpg

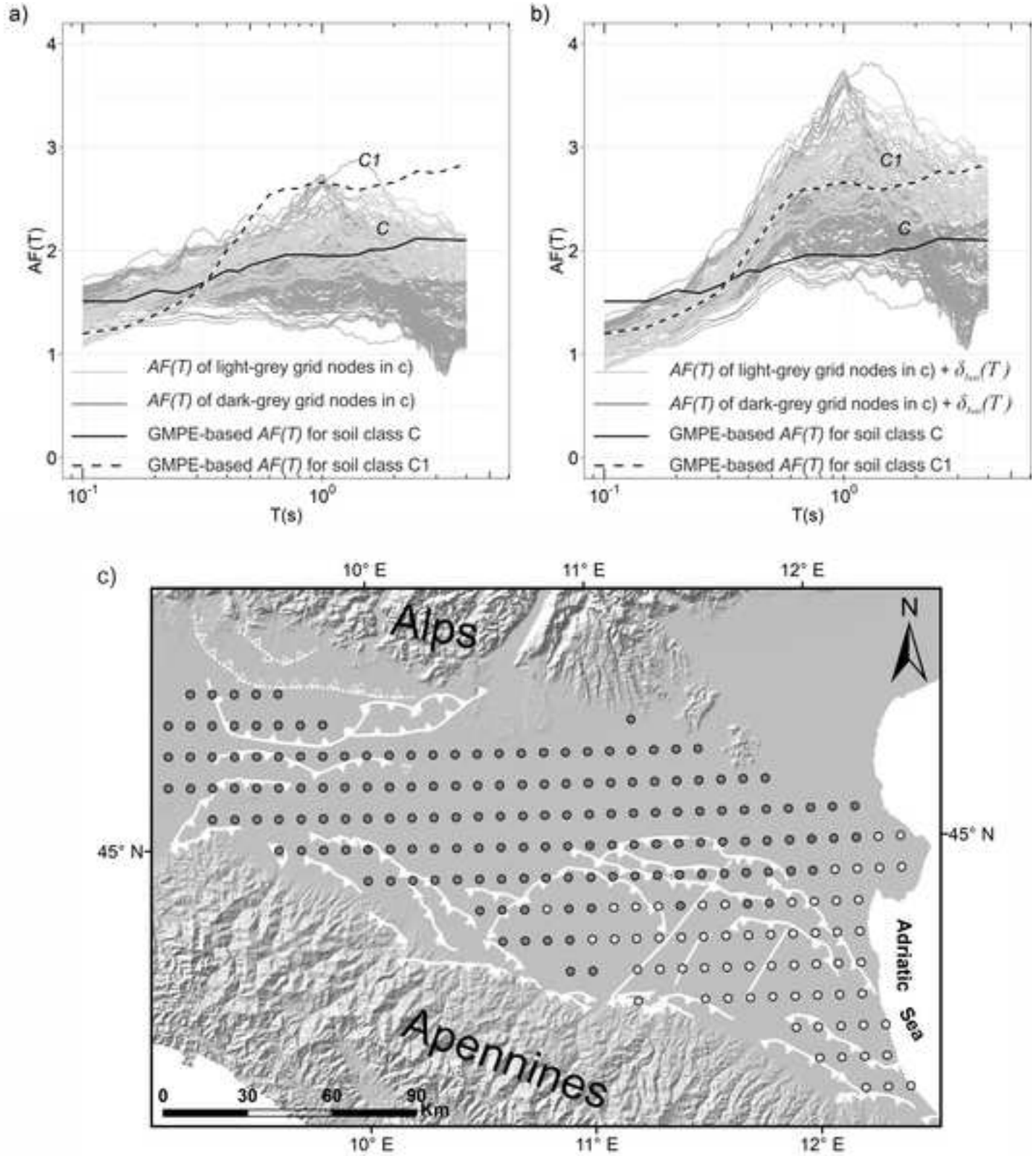

Electronic supplement

Article title: *New insights into long-period (>1s) seismic amplification effects in deep sedimentary basins: A case of the Po Plain basin of northern Italy*

Authors:

Mascandola C., Barani S., Massa M., Albarello D.

Table S1. List of acceleration time histories considered in the present study. *Lat.*, *Long.*, and *Depth* are the coordinates of the hypocenters; M_w is moment magnitude; R_{epi} stands for epicentral distance; $V_{S,30}$ is the average shear-wave velocity in the first 30 m of subsoil. PGA and PGV are the Peak Ground Acceleration and the Peak Ground Velocity, respectively. $I_\gamma = PGV/V_{S,30}$ is the shear strain index (e.g., Idriss, 2011). SoF is the Style of Faulting. The column "Area" reports an identifier indicating the zone where the selected time histories are applied (1: moderate-to-high seismic hazard zone; 2: low-to-moderate hazard zone; 3: low hazard zone; 4: very low hazard zone). For more details about the zones and the selection of input motions refer to Mascandola et al. (2020), where the selected records are supplied.

Network codes: IT (Italian Strong Motion Network - Italy); HI (ITSAK Strong Motion Network - Greece); TK (Turkish National Strong Motion Network - Turkey); CI (Southern California Seismic Network - USA); CE (California Strong Motion Instrumentation Program - USA); BO (Bosai-Ken Network - Japan).

Earthquake Name	Country	Date (YYYYMMDD)	Time (UTC)	Lat. [°]	Long. [°]	*Depth (km)*	M_w	R_{epi} (km)	Station code	Station Name	*Network code*	$V_{S,30}$ [m/s]	PGA [cm/s^2]	PGV [cm/s]	I_γ	SoF	Database	Area
Greece	Greece	19990907	11:56:49	38.122	23.582	9.40	5.9	19.7	ATH4	-	HI	1020	118.7	8.9	8.73E-05	NF	ESM	1
Central Italy	Italy	20090407	09:26:28	42.336	13.387	9.60	5.1	5.5	AQP	L'Aquila-V.Aterno-M.Pettino	IT	836	37.1	1.6	1.91E-05	NF	ESM	4
Central Italy	Italy	20090407	17:47:37	42.303	13.486	17.10	5.5	13.2	AQP	L'Aquila-V.Aterno-M.Pettino	IT	836	92.1	4.3	5.14E-05	NF	ESM	1
Central Italy	Italy	20090407	21:34:29	42.372	13.374	7.20	4.5	1.4	AQP	L'Aquila-V.Aterno-M.Pettino	IT	836	166.4	5.7	6.82E-05	NF	ESM	1
Central Italy	Italy	20090409	19:38:16	42.504	13.35	9.30	5.2	13.5	AQP	L'Aquila-V.Aterno-M.Pettino	IT	836	55.8	1.9	2.27E-05	NF	ESM	4
Central Italy	Italy	20090703	22:56:50	42.397	13.39	10.80	4.1	2.3	AQP	L'Aquila-V.Aterno-M.Pettino	IT	836	19.3	0.7	8.37E-06	NF	ESM	4
Central Italy	Italy	20161030	06:40:18	42.8322	13.1107	9.20	6.5	62.7	FMG	Fiamignano	IT	790	25.2	4.1	5.19E-05	NF	ESM	3
Central Italy	Italy	20071021	03:55:36	42.401	12.963	8.00	4.2	19.5	FMG	Fiamignano	IT	790	30.3	0.5	6.33E-06	NF	ESM	2
Southern Italy	Italy	19980909	11:28:00	39.979	16.026	7.40	5.6	18	LRS	Lauria	IT	1024	161.9	12.5	1.22E-04	NF	ESM	1,3
Cosenza	Italy	20121025	23:05:24	39.8747	16.0158	9.70	5	2.4	MRM	Mormanno	IT	1906	182.4	11.3	5.93E-05	NF	ESM	3
Southern Italy	Italy	20130216	21:16:09	41.7143	13.5697	17.10	4.8	21.2	PSC	Pescasseroli	IT	1000	52.1	1.9	1.90E-05	NF	ESM	2
Central Italy	Italy	20161030	06:40:18	42.8322	13.1107	9.20	6.5	70.6	SDM	S. Demetrio nei Vestini	IT	752	29.8	4.2	5.59E-05	NF	ESM	4
Central Italy	Italy	20170118	10:14:12	42.531	13.2838	9.60	5.5	35	SDM	S. Demetrio nei Vestini	IT	752	28.2	1.1	1.46E-05	NF	ESM	2,4
Friuli	Italy	19760911	16:31:10	46.275	13.198	9.80	5.2	7	TRC	Tarcento	IT	780	240.9	6.8	8.72E-05	TF	ESM	1
Turkey	Turkey	19990913	11:55:27	40.75	30.079	10.40	5.8	13.8	4101	AI_004_IZT	TK	827	317.3	15.1	1.83E-04	NF	ESM	1,2,4
Northridge	California	19940117	12:31	34.2057	-118.5539	17.50	6.7	19	WNS	LA - Wonderland Ave	CI	1223	138.2	12.2	9.98E-05	TF	PEER NGA-West2	2
Coyote Lake	California	19790806	17:05	37.065	-121.49	8.00	5.7	12.6	47379	Gilroy Array #1	CE	1428	103.9	7.6	5.36E-05	SS	PEER NGA-West2	1
Sierra Madre	California	19910628	-	34.2591	-118.001	12.00	5.6	39.6	24047	Vasquez Rocks Park	CE	996	101.2	2.8	2.80E-05	TF	PEER NGA-West2	1
Chi-Chi	Taiwan	19990920	21:46	23.6	120.82	18.00	6.2	81.4	TTN042	Awano	BO	845	26.6	2.7	3.18E-05	SS	PEER NGA-West2	3
Chi-Chi	Taiwan	19990922	00:14	23.81	121.08	10.00	6.2	78.8	CHY102	-	-	804	58.3	2.4	3.03E-05	TF	PEER NGA-West2	2

Tottori	Giappone	20001006	04:30	35.275	133.35	13.00	6.6	25.6	OKYH07	Shingo	BO	940	145.9	11.1	1.18E-04	SS	PEER NGA-West2	3
Tottori	Giappone	20001006	04:30	35.275	133.35	13.00	6.6	31.4	SMNH10	Mihonoseki	BO	967	199.7	15.7	1.62E-04	SS	PEER NGA-West2	2,3
Umbria	Italy	19840429	05:02	43.204	12.585	9.00	5.6	17.1	GBB	Gubbio	IT	922	68.3	2.9	3.19E-05	NF	PEER NGA-West2	3,4
Iwate	Giappone	20080613	23:43	39.027	140.878	6.50	6.9	84.3	IWTH18	Kawai-S	BO	892	129.7	3.8	4.31E-05	TF	PEER NGA-West2	2
Loma Prieta	California	19891018	00:05	37.0407	-121.8829	17.48	6.9	92.2	58790	Piedmont Jr High School Grounds	CE	895	74.6	9.2	1.03E-04	TP	PEER NGA-West2	4
Loma Prieta	California	19891018	00:05	37.0407	-121.8829	17.48	6.9	96.3	58131	SF - Pacific Heights	CE	1250	53.5	11.0	8.79E-05	TP	PEER NGA-West2	4
Loma Prieta	California	19891018	00:05	37.0407	-121.8829	17.48	6.9	83.5	58539	So. San Francisco, Sierra Pt.	CE	1021	79.7	7.7	7.52E-05	TP	PEER NGA-West2	2
San Fernando	California	19710209	14:00	34.44	-118.41	13.00	6.6	39.2	266	Pasadena - Old Seismo Lab	-	969	142.3	9.9	1.02E-04	TF	PEER NGA-West2	2
Chi-Chi	Taiwan	19990922	00:14	23.81	121.08	10.00	6.2	92.3	TTN042	-	-	845	43.5	2.8	3.26E-05	TF	PEER NGA-West2	3
Tottori	Giappone	20001006	04:30	35.275	133.35	13.00	6.6	109.7	HYG007	Haga	BO	761	35.1	1.3	1.73E-05	SS	PEER NGA-West2	1
Niigata	Giappone	20041023	08:56	37.307	138.839	10.60	6.6	109.3	TCGH14	Awano	BO	849	31.02	0.9	1.09E-05	TF	PEER NGA-West2	3
Chuetsu-oki	Giappone	20070716	10:13	37.5382	138.6174	9.00	6.8	113.8	TCGH17	Fujhara2	BO	1433	25.3	0.7	4.75E-06	TF	PEER NGA-West2	3,4
Iwate	Giappone	20080613	23:43	39.027	140.878	6.5	6.9	119.3	IWTH14	Taro	BO	816	143.7	3.7	4.47E-05	TF	PEER NGA-West2	1

References

Idriss, I. M. (2011). Use of $V_{S,30}$ to represent local site conditions, in 4th LASPEI/IAEE International Symposium Effects of Surface Geology on Strong Ground Motions, Santa Barbara, CA.

Mascandola, C., Barani, S., Massa, M., Paolucci, E., and Albarello, D. (2020). Clustering analysis of probabilistic seismic hazard for the selection of ground motion time histories in vast areas. Bulletin of Earthquake Engineering, 1-20.